remote sensing

MDPI

Article

Transport and Variability of Tropospheric Ozone over Oceania and Southern Pacific during the 2019–20 Australian Bushfires

Nelson Bègue [1,*], Hassan Bencherif [1], Fabrice Jégou [2], Hélène Vérèmes [1], Sergey Khaykin [3], Gisèle Krysztofiak [2], Thierry Portafaix [1], Valentin Duflot [1], Alexandre Baron [1], Gwenaël Berthet [2], Corinna Kloss [2], Guillaume Payen [4], Philippe Keckhut [3], Pierre-François Coheur [5], Cathy Clerbaux [3,5], Dan Smale [6], John Robinson [6], Richard Querel [6] and Penny Smale [6]

1 Laboratoire de l'Atmosphère et des Cyclones (LACy, UMR 8105 CNRS, Université de la Réunion, Météo-France), Université de La Réunion, 97400 Saint-Denis de La Réunion, France; hassan.bencherif@univ-reunion.fr (H.B.); helene.veremes@univ-reunion.fr (H.V.); thierry.portafaix@univ-reunion.fr (T.P.); valentin.duflot@univ-reunion.fr (V.D.); alexandre.baron@univ-reunion.fr (A.B.)
2 Laboratoire de Physique et Chimie de l'Environnement et de l'Espace (LPC2E), Université d'Orléans, 45100 Orléans, France; fabrice.jegou@cnrs-orleans.fr (F.J.); gisele.krysztofiak@cnrs-orleans.fr (G.K.); gwenael.berthet@cnrs-orleans.fr (G.B.); corinna.kloss@cnrs-orleans.fr (C.K.)
3 LATMOS/IPSL, UVSQ Université Paris-Saclay, Sorbonne Université, CNRS, 75000 Paris, France; sergey.khaykin@latmos.ipsl.fr (S.K.); keckhut@latmos.ipsl.fr (P.K.); Cathy.Clerbaux@ulb.be (C.C.)
4 Observatoire des Sciences de l'Univers de La Réunion (OSU-Réunion), UAR 3365, Université de la Réunion, CNRS, Météo-France, 97400 Saint-Denis de La Réunion, France; guillaume.payen@univ-reunion.fr
5 Spectroscopy, Quantum Chemistry and Atmospheric Remote Sensing (SQUARES), Université libre de Bruxelles (ULB), 1050 Brussels, Belgium; pfcoheur@ulb.ac.be
6 National Institute of Water & Atmospheric Research (NIWA), Omakau 9377, New Zealand; dan.smale@niwa.co.nz (D.S.); john.robinson@niwa.co.nz (J.R.); richard.querel@niwa.co.nz (R.Q.); penny.smale@niwa.co.nz (P.S.)
* Correspondence: nelson.begue@univ-reunion.fr

Abstract: The present study contributes to the scientific effort for a better understanding of the potential of the Australian biomass burning events to influence tropospheric trace gas abundances at the regional scale. In order to exclude the influence of the long-range transport of ozone precursors from biomass burning plumes originating from Southern America and Africa, the analysis of the Australian smoke plume has been driven over the period December 2019 to January 2020. This study uses satellite (IASI, MLS, MODIS, CALIOP) and ground-based (sun-photometer, FTIR, ozone radiosondes) observations. The highest values of aerosol optical depth (AOD) and carbon monoxide total columns are observed over Southern and Central Australia. Transport is responsible for the spatial and temporal distributions of aerosols and carbon monoxide over Australia, and also the transport of the smoke plume outside the continent. The dispersion of the tropospheric smoke plume over Oceania and Southern Pacific extends from tropical to extratropical latitudes. Ozone radiosonde measurements performed at Samoa (14.4°S, 170.6°W) and Lauder (45.0°S, 169.4°E) indicate an increase in mid-tropospheric ozone (6–9 km) (from 10% to 43%) linked to the Australian biomass burning plume. This increase in mid-tropospheric ozone induced by the transport of the smoke plume was found to be consistent with MLS observations over the tropical and extratropical latitudes. The smoke plume over the Southern Pacific was organized as a stretchable anticyclonic rolling which impacted the ozone variability in the tropical and subtropical upper-troposphere over Oceania. This is corroborated by the ozone profile measurements at Samoa which exhibit an enhanced ozone layer (29%) in the upper-troposphere. Our results suggest that the transport of Australian biomass burning plumes have significantly impacted the vertical distribution of ozone in the mid-troposphere southern tropical to extratropical latitudes during the 2019–20 extreme Australian bushfires.

Keywords: tropospheric ozone; Australian fires; carbon monoxide; plume transport

Citation: Bègue, N.; Bencherif, H.; Jégou, F.; Vérèmes, H.; Khaykin, S.; Krysztofiak, G.; Portafaix, T.; Duflot, V.; Baron, A.; Berthet, G.; et al. Transport and Variability of Tropospheric Ozone over Oceania and Southern Pacific during the 2019–20 Australian Bushfires. *Remote Sens.* **2021**, *13*, 3092. https://doi.org/10.3390/rs13163092

Academic Editor: Fred Moshary

Received: 29 June 2021
Accepted: 1 August 2021
Published: 5 August 2021

1. Introduction

Biomass burning is a significant source of aerosols and active trace gases that impact the atmospheric composition from local to global scales, with consequences for tropospheric ozone production and budget. Tropospheric ozone presents a serious environmental issue due to its negative impact on human health and Earth's climate. Tropospheric ozone is predominantly produced by photochemical reactions involving precursors generated by natural processes, and to a much larger extent, by anthropogenic activities [1]. Previous works have showed that large amounts of ozone precursors such as carbon monoxide (CO) are injected throughout the troposphere during the biomass burning activity [2–4]. Generally, ozone radiative forcing depends on its vertical distribution. In the troposphere, ozone is a greenhouse gas that plays a key role in radiative forcing and indeed in climate change [5]. Aerosols or photochemical compounds produced during biomass burning events have a large radiative effect on climate but are still scarcely quantified in the literature. This is especially true in the southern hemisphere due to the low number of observational stations, in comparison with the northern hemisphere.

The bulk of biomass burning activity in the southern hemisphere occurs in the Southern American and Southern African regions [6–8] from July to November. High concentrations of ozone precursors and aerosols from these fires can be transported far from the source regions [9]. Based on satellite observations and ground-based measurements at Lauder (45.0°S, 169.4°E), Edwards et al. [10] showed that intercontinental transport of biomass burning pollution from Africa and South America often determines the local air-quality over this site. They showed that the fraction of the pollutants following this pathway is estimated to be less than 10% of the total emission in South America and Africa. By combining 10 years of ozone radiosondes performed at several Tropical Pacific sites and back-trajectory modeling, Oltmans et al. [11] pointed out the contribution of intercontinental transport of biomass burning plume from Africa and South America on tropospheric ozone variability over the Southern Pacific between September and November. Oltmans et al. [11] did not exclude that Australian and Indonesian biomass burning activity may have also contributed to the tropospheric ozone variability over Oceania and the Southern Pacific. Pak et al. [12] reported aircraft missions conducted over southeastern Australia and Tasmania in parallel with the Southern African Regional Science Initiative (SAFARI 2000) campaign in Africa. These large-scale studies in Africa and South America have provided valuable insight into the impact of the long-range transport of the smoke plume on the composition of the atmosphere over Oceania. Despite these studies, there is still a need for a better scientific understanding of the influence of biomass burning on atmospheric composition and air-quality [13], particularly around Australia.

The vast majority of the Australian biomass burning activity takes place in the northern tropical part of the continent, where the ecosystem is dominated by savannah. These fires are responsible for more than half of the land area burned between September and January [14]. Previous works revealed that emissions from fires in the savannah regions of Northern Australia can be considered as the most significant regional source of greenhouse and other trace gases, as well as atmospheric aerosols [15–17]. Nevertheless, the intensity of these fires is low to moderate, generally limited to the grass layer [17–19]. The propagation of the smoke plumes from these fires is mainly limited to the planetary boundary layer and to the northwest over the Timon Sea [15,20]. Although the vast majority of the continent's fires occur in the Northern region of Australia, the most devastating fires burn in the densely populated Southern regions. Southeastern Australia has a combination of climate conditions and vegetation type that makes it prone to severe wildfires [21]. Sullivan et al. [22] reported that extreme fire events occurred in most recent years over southeastern Australia but were generally more extensive and severe following extended drought, typically associated with El Niño events. The extreme fire events occurring over southeastern Australia can trigger the development of convection, which leads to the lifting of aerosols and trace gases to high altitudes. Moist convection can sometimes occur in the fire plume and lead to the formation of convective clouds (pyro-cumulus)

or thunderstorms (pyro-cumulonimbus) [23]. These phenomena are widely known as pyro-convection events [24]. The vertical transport of the smoke plume is, therefore, due to a combination of extreme heat energy release from the fire and convection. Under favorable meteorological conditions, pyro-convection events have the potential to inject soot and smoke directly into the stratosphere. Southeastern Australia has a long history of severe pyro-convection events which have significantly impacted the composition of the stratosphere at regional and global scales. In the past two decades, pyro-convection events have impacted southeastern Australia in 2003 [24–27], 2006 [28,29] and 2009 (colloquially known as "Black Saturday") [30–33]. Recently, this list has grown as a result of a new pyro-convection event occurring during the 2019–20 fire season in eastern and southeastern Australia (colloquially known as "Black Summer") [34–37].

Nolan et al. [38] reported that the 2019–20 fire season in eastern and southeastern Australia was unprecedented in the size and number of fires. Boer et al. [39] estimated that the area burnt during this fire season was about six million hectares. It was also reported that Eastern Australia experienced severe drought before and during this fire season (www.bom.gov.au/climate/maps/ (accessed on 2 August 2021) [38]. The meteorological conditions were favorable to extreme fires leading to pyro-convection events between New Year's Eve and mid-January. Khaykin et al. [36] reported that the 2019–20 Australian wildfires caused a massive injection of combustion products into the stratosphere that led to a persistent planetary-scale perturbation of all stratospheric climate-relevant variables. The perturbation induced by the 2019–20 Australian wildfires in the stratosphere put this event on a par with the strongest volcanic eruptions of the last 25 years [35,36,40]. The gases and aerosols injected into the stratosphere were advected by westerly winds and dispersed across all the southern hemisphere's extratropical latitudes [41]. The smoke plume returned back to Australia in less than two weeks by passing over South America [37]. Based on satellite observations and European Centre for Medium-Range Weather Forecast (ECMWF) operational data, Khaykin et al. [36] revealed that this extreme event enabled the discovery of a striking atmospheric phenomenon, a persistent synoptic-scale anticyclone, which acts to confine the carbon-rich aerosol clouds during their solar-driven rise. In this way, highly-concentrated absorbing aerosols are lofted into the middle stratosphere, which prolongs their stratospheric residence time and radiative effects on climate. Most of these previous works report on the investigation on the perturbation of stratospheric composition, and on the dynamical circulation induced by the 2019–20 Australian wildfires.

In contrast, relatively little attention has been paid to smoke emissions in the troposphere during these extreme wildfires. Few studies on the influence of the smoke emissions from southeastern and eastern Australia on the tropospheric variability of aerosols and trace gases were undertaken [11,40,42,43]. This is fairly surprising in view of the potential of biomass burning activity to change the physico-chemical composition in the troposphere at the local and regional scale [44,45]. Based on ozone observations from LiDAR and radiosondes over Reunion Island, Clain et al. [44] showed a significant annual increase in tropospheric ozone over Reunion Island during the August–November period, in parallel with the biomass burning season in Southern Africa and Madagascar. High concentrations of ozone precursors from these fires are vented into the free troposphere by convection and are subsequently advected into the Indian Ocean region by westerly winds.

The present work reports on the characteristics of the tropospheric smoke plumes originating from southeastern and eastern Australian during the 2019–20 fire season. It aims to investigate the tropospheric ozone variability over Oceania and the Southern Pacific induced by the transport of the Australian smoke plume during the 2019–20 fire season. The chemical and optical properties of the smoke plume are mainly inferred from ground-based observations collected in the framework of international networks. Even though Kloss et al. [40] showed that the Australian fire season of 2019–20 has already significantly impacted fire trace gas abundances in the southern hemisphere's troposphere starting from September/October 2019, here we focus on the peak phase of the fire events (From December 2019 to January 2020). This is carried out to exclude the possible impact

of ozone precursors from biomass burning plumes originating from Southern America and Africa [10].

The paper is organized as follows: Section 2 describes the ground-based and space-borne observations used for the investigation of the tropospheric smoke plume. A review of the spatio-temporal evolution of the CO and aerosols' total column over Australia is provided in Section 3. An analysis of the tropospheric smoke plume is also provided in Section 3. The discussion on the tropospheric ozone variability over Oceania and Southern Pacific is presented in Section 4. A summary and the perspectives of this study are finally given in Section 5.

2. Instruments and Data Sets

The characteristics of the fire emissions were investigated using all available observations of trace gases (mainly CO and ozone) and aerosols over Australia and its surroundings. The data set used in this study consists of ground-based and space-borne observations. Given the lifetime of CO (~1 to 3 months in the troposphere), this latter is often used as tracer to study the long-range transport of biomass burning [4,46,47]. CO concentration is associated with many tropospheric polluting gases such as tropospheric ozone. To investigate the tropospheric ozone variability induced by the Australian fires, it is important to have an idea about the background situation when the atmosphere is not undergoing major disturbances (e.g, volcanic eruptions, pyro-convection outbreaks). In the present work, the background period is defined as the period ranging from January 2010 to December 2018. The previously reported pyro-convection events in southeastern Australia were discarded from the background values.

2.1. Ozone and CO Measurements

2.1.1. FTIR

Total column and volume mixing ratio profiles of trace gases such as CO and ozone were retrieved with high accuracy and precision from ground-based Fourier transform infrared (FTIR) spectrometers [48,49]. In the present study, we use FTIR ozone and CO observations taken at Lauder (New Zealand). These measurements have been taken since the early 1990s within the framework of the NDACC (Network for the Detection of Atmospheric Composition Change) network [50]. The measurements are taken on clear-sky days, throughout the day, using a Bruker high-resolution spectrometer over a wide spectral range (around 600–4500 cm^{-1}). A detailed description of the ozone and CO retrieval algorithms is given by Vigouroux et al. [48] and Morgenstern et al. [51]; they are briefly summarized here. The CO and ozone total column amounts and volume mixing ratio profiles are retrieved using the spectral least-squares fitting (SFIT) algorithm [52,53]. This algorithm is based on the optimal estimation method developed by Rodgers [54]. FTIR retrievals are performed on a 48-layer atmosphere (0.37–100 km asl) of which 15 layers are between 0.37 and 10 km. The retrievals use a static a priori originating from WACCM 4 (Whole Atmosphere Community Climate Model, version 4) model simulations [55]. The retrievals are constrained using regularization criteria (a priori covariance matrix and spectrum signal to noise ratio). This regularization step is taken in order to obtain stable physically realistic retrievals with reasonable degrees of freedom (DoFs) for the signal. Across the whole measurement period at Lauder, the average DoFs value in the troposphere was 1.50 and 2.31 for ozone and CO, respectively.

The CO and ozone total columns and volume mixing ratio profiles used in this study were downloaded from the NDACC database (http://www.ndacc.org, accessed on 21 June 2021).

2.1.2. Ozone Radiosondes

The ozonesondes provide ozone profiles from ground up to burst-balloon altitude, which is around 30–35 km, with a vertical resolution of 150 m. The dataset used in this

study includes ozone profiles recorded at Lauder (45.0°S, 169.4°E) and Samoa (14.4°S, 170.6°W) by balloon-sonde experiments (location of these two sites is reported in Figure 1).

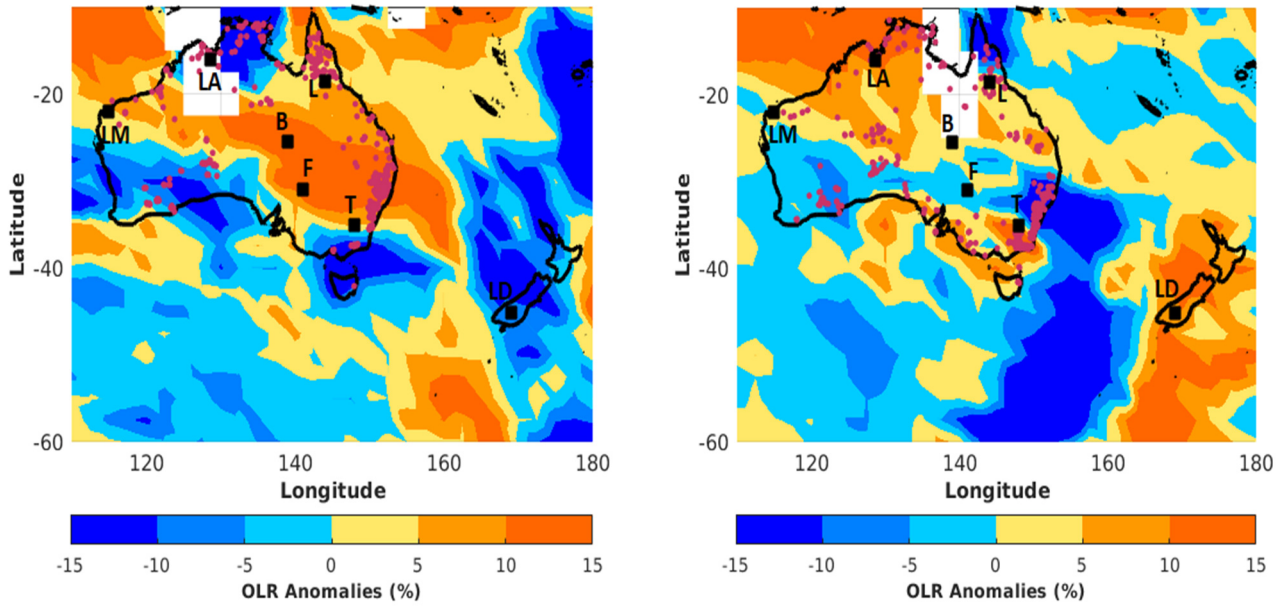

Figure 1. Daily Outgoing Longwave Radiation anomalies obtained from NCEP analysis on (**a**) 19 December 2019 and (**b**) 31 December 2019. The red dots correspond to location of fires obtained from MODIS. The locations of Lake Argyle, Lucinda, Learmonth, Birdsville, Fowlers Gap, Tumbarumba and Lauder sites are indicated by LA, L, LM, B, F, T and LD, respectively.

The ozonesonde measurements at Samoa were initiated in 1989 in the framework of several measurement programs, such as Pacific Exploratory Mission [11]. Samoa has been included in the SHADOZ (Southern Hemisphere ADditional Ozone sondes) network since 1998, and the frequency of radiosonde experiments increased to become weekly. Through the SHADOZ project a systematic effort was made to collect regular ozone profile data from stations throughout the tropical and subtropical regions of the southern hemisphere. Details concerning the SHADOZ program are available from Thompson et al. [56]. The balloon-borne sonde equipment used at Samoa consists of an electrochemical concentration cell (ECC) ozonesonde which measures the oxidation of a potassium iodine (KI) solution by ozone [57]. This chemical reaction allows the retrieval of the ozone partial pressure profile. The ECC ozonesonde is coupled with a standard radiosonde to obtain meteorological parameters. Thompson et al. [58] have reported that ECC sondes have an absolute accuracy of 5%. In order to check the quality of the data, the Samoa ozonesonde system was part of the JOSIE (Julich Ozone Sonde Intercomparison Experiment) process. This intercomparison campaign, which was under the World Meteorology Organization (WMO) initiative, aimed to assess the performance of radiosonde systems through an intercomparison experiment using a standard reference instrument [59]. A total of 259 ozone profiles performed at Samoa from 2010 to 2020 were considered in the present study, and were downloaded from the SHADOZ database: https://tropo.gsfc.nasa.gov/shadoz/ (accessed on 21 June 2021).

The ozone radiosondes at Lauder have been routinely performed in the framework of the NDACC network since 1986. At Lauder, the balloon-sonde is also equipped with an ECC ozonesonde operating with 0.5% buffered KI cathode solution [60]. Bodeker et al. [61] compared the integrated ozone profile with the total column of ozone measured by co-located Dobson spectrophotometer. They found less than 5% discrepancy. The Lauder data set used in this study consists of 522 ozone profiles during the same period of time,

2010–2020. The ozone profiles recorded at Lauder are available on the NDACC website (http://www.ndacc.org, accessed on 21 June 2021).

2.1.3. Satellite Date

MLS

The Microwave Limb Sounder (MLS) instrument onboard Aura has been operating since August 2004 [62]. It is a thermal-emission microwave limb sounder that measures mixing ratio profiles from the upper-troposphere to the mesosphere of a number of chemical species (e.g, CO, ozone, water vapour) from limb scans taken in the direction ahead of the Aura satellite orbital track. The orbit is sun-synchronous, so that the observations are always made at the same two local times for a given latitude. The output of the radiometers is analyzed by banks of filters. The ozone profiles are retrieved using radiances at 240 GHz. The radiances reported by the filter banks are used as input to a software package [63] which estimates profiles of temperature, and profiles of the mixing ratios of the targeted chemical species.

In the present work, we used the MLS version 4.2 Ozone Mixing Ratio (OMR). All MLS v4.2 retrieval quality flags (quality, status, convergence, and precision) were properly adhered to for all of our analyses. The MLS v4.2 measurements, including data quality and quality flags, are described in the MLS data quality document (http://mls.jpl.nasa.gov/data/v4-2_data_quality_document.pdf, accessed on 6 June 2021) and by Livesey et al. [63]. Generally, recommended pressure levels for science applications with ozone MLS data range from 0.0215 to 261 hPa. A validation study of the MLS v4.2 OMR with ozone radiosonde over the Tibetan Plateau was undertaken by Yan et al. [64]. Their results suggest that MLS v4.2 represents a substantial improvement in ozone retrievals throughout the upper troposphere in comparison with the previous versions (accuracy of 20 ppbv at 215 hPa and 30 ppbv at 100 hPa). The OMR profiles from MLS were obtained from the Atmospheric Composition Data and Information Services Center (ACDISC) archive (ftp://acdisc.gsfc.nasa.gov, accessed on 21 June 2021) hosted by the NASA Goddard Space Flight Center.

IASI

The Infrared Atmospheric Sounding Interferometer (IASI) onboard the Meteorological Operational (MetOp) satellite measures chemical species (e.g., ozone, sulfur dioxide, CO) on a global scale [65–67]. The IASI atmospheric sounder uses a Fourier transform spectrometer, which measures the infrared radiation emitted by the Earth's surface and the atmosphere, covering wavelengths from 6.62 to 15.5 μm, allowing for day and night measurements. It was designed for global observations with a vertical range covering the troposphere and the lower stratosphere.

Retrieval of CO and O_3 total and partial columns occur in near real-time from the nadir radiance spectra measured by the instrument in the thermal infrared (TIR) spectral range. Global distributions are obtained at around 9:30 AM and PM (local time) using a dedicated radiative transfer and retrieval software for the IASI products: The Fast-Optimal Retrievals on Layers for IASI (FORLI-CO and FORLI-O3). A full description is given by Hurtmans et al. [68], and a cloud filtering is applied to the data set before further exploitation. Global distributions of CO columns were evaluated with correlative observations available from other nadir looking TIR missions. On average, George et al. (2009) found total column discrepancies of about 7% in comparison with three other sounders. The valuable nature of CO total column observations from IASI for the study of long-range transport of the smoke plume during biomass burning events is well documented in previous research [47,69]. IASI tropospheric ozone from FORLI-O3 has been extensively validated and compared with available ground-based, aircraft, ozone radiosondes, and other satellite observations [69–71]. These analyses show that IASI underestimates tropospheric ozone by 12% to 14% in the mid-latitudes and tropics. In the present study, we used CO and ozone columns from IASI instruments on Metop-A and Metop-B, which have

been operating since 2006 and 2012, respectively. The IASI products used in this work are available on the AERIS platform: https://iasi.aeris-data.fr/ (accessed on 27 July 2021).

2.2. Aerosols Data Sets

2.2.1. Sun-Photometer CIMEL

The ground-based sites selected to investigate the aerosol variability over Australia include 6 AERONET (Aerosols Robotic NETwork) sites strategically deployed over the continent (Figure 1): Lake Argyle (16.1°S; 128.7°E), Lucinda (18.5°S, 146.4°E), Learmonth (22.1°S, 114.1°E), Birdsville (25.8°S, 139.3°E), Fowlers Gap (31.1°S, 141.7°E) and Tumbarumba (35.7°S, 147.9°E). The selected sites allow an overview of the latitudinal distribution of AOD in Australia. As mentioned here above, all available observations recorded between January 2010 and December 2018 have been used to define the background values for each site. Given that the Tumbarumba site has been operating since 2019, we used aerosol optical depth (AOD) data recorded at Canberra (35.1°S, 149.0°E—shut off since 2017) to build the background values. This approach was recently used and validated by Yang et al. [72].

A detailed description of the CIMEL sunphotometer of the AERONET network and the associated data retrieval is given by Holben et al. [73] and it is summarized hereafter. The direct solar extinction and diffuse sky radiance measurements are used to compute AOD and to retrieve aerosol size-distribution using the methodology of Dubovik and King [74]. The measurements are performed under cloud-free and daytime conditions at 15 min intervals. Previous works showed that estimated uncertainty in AOD measurements under cloud free conditions ranges from 0.01 to 0.02 [75]. The AOD values presented in this work are selected at Level 1.5 (Version 3) since level 2 data were not yet available at the time of this study. Giles et al. [76] showed that the new level 1.5 (version 3) AOD data are statistically very close to version 2 level 2.0. The level 1.5 of AOD data with version 3 refers now to near real-time automatic cloud screening and automatic instrument anomaly quality controls. We also note that the new level 1.5 (version 3) AOD data have been validated and used in recent works [48,77,78]. The AOD data used in the present study were downloaded from the AERONET web site: http://aeronet.gsfc.nasa.gov (accessed on 2 August 2021).

2.2.2. Satellite Data

CALIOP

Observations from the Cloud-Aerosol Lidar with Orthogonal Polarization (CALIOP) onboard the Cloud-Aerosol Lidar and Infrared Pathfinder Satellite Observation (CALIPSO) were used to study the transport of the smoke aerosol layers. CALIPSO flies in a sun-synchronous polar orbit since 2006 with a cycle of 16 days. A detailed description of CALIPSO is given by Winker et al. [79]. In the present work, we also used the CALIOP version 4.1 AOD products level 2 (80, 81). Young et al. [80] reported extensive upgrades to the algorithms used to retrieve the extinction and AOD with CALIOP version 4.1 data products. A validation study of the CALIOP 4.1 AOD data products with AERONET and MODIS observations was reported by Kim et al. [81]. They showed that the aforementioned AOD discrepancies between CALIOP and instruments are reduced in version 4 compared to version 3. The CALIOP version 4 AOD data product has been used previously for optical characterization of aerosol plume over biomass burning or dust sources [82–84]. The CALIOP data were obtained from the ACDISC data archive (ftp://acdisc.gsfc.nasa.gov, accessed on 16 July 2021) hosted by NASA Goddard Space Flight Center.

GOME-2

The GOME-2 (Global Ozone Monitoring Experiment) onboard the MetOp satellites is a nadir viewing scanning spectrometer which provides global coverage of the sunlit part of the atmosphere with a spatial coverage of 80 × 40 km [85]. The absorbing aerosol index (AAI) data from GOME-2 onboard MetOp-B were used to describe the transport of the Australian biomass burning plume. This index allows the detection of absorbing aerosols

through the spectral difference between 340 nm and 380 nm. The AAI index has provided information about smoke plume horizontal distribution over land and ocean surface in many studies [25,28,31]. The AAI data were downloaded from: https://www.temis.nl/airpollution/absaai/ (accessed on 21 June 2021).

2.3. MODIS Fire Data

The location of fires is derived from the Moderate Resolution Imaging Spectroradiometer (MODIS) sensors onboard the Aqua and Terra platforms launched by NASA in 1999 and 2002, respectively. Previous works confirm that MODIS can be considered as one of the primary reference instruments for fire detection and monitoring [15,47,86]. MODIS performs measurements at 36 different bands ranging from 0.4 to 14.4 µm, and has infrared channels specifically designed for fire observations. Aqua and Terra satellites have sun-synchronous orbits. Owing to its wide ground scan (2330 km) capability, the MODIS instrument takes one to two days to observe each point on the Earth surface, with a spatial resolution ranging from 0.25 km to 1.00 km, depending on the channels used. The orbit of Aqua and Terra is timed so that it passes over the equator from north to south in the morning. Kaufman et al. [87] reported that the principle of fire detection by MODIS is based on a comparison of the brightness temperatures of two channels, i.e., 4 µm and 11 µm, recorded for each 1 km^2 pixel. A fire is, hence, attributed to the pixel when the difference between the brightness temperatures of the 4 µm and 11 µm channels are above a certain threshold. The MODIS fire products used in this study to investigate fire distributions across Australia during the 2019–20 fire season were downloaded from the NASA Earth Data platform: https://earthdata.nasa.gov/earth-observation-data/near-real-time/firms/active-fire-data (accessed on 10 June 2021).

3. Australian Biomass Burning Event

3.1. CO and Aerosols Total Columns over Australia

Southeastern and eastern Australia was impacted by a severe heat wave on December 2019 [35,88]. This heat wave led to drought conditions in New South Wales, Victoria and Queensland. At the beginning of December, fires were located over the northwestern side of Australia, and moved to the eastern and southeastern side from mid-December. The daily location of fire pixels detected from MODIS and daily OLR (Outgoing Longwave Radiation) anomalies from NCEP analysis on 19 and 31 December are depicted on Figure 1a,b, respectively. On 19 December, fires are mainly located over eastern Australia within a region of positive OLR anomalies (greater than 15%), as is illustrated on Figure 1a. The prolonged drought and drying of the land may have increased the risk of extensive fires, as suggested in previous similar published works [25,31]. On 31 December, the maximum intensity of fire pixels was concentrated over southeastern Australia (Figure 1b). Figure 1b reveals that negative OLR anomalies (greater than 15%, in absolute value) are observed over southeastern Australia. It is conceivable that an intensification of the fire in this region has forced the formation of deep convection [25]. We note that the most intense fires were located over southeastern Australia with FRP (Fire Radiation Power) values ranging from 1500 to 2500 MW (particularly in the state of Victoria) between 30 December 2019 and 12 January 2020. Conversely, the northern region (between 10°S and 22°S) is not impacted by the intense fires (FRP values less than 100 MW) from 1 December 2019 to 31 January 2020.

The latitudinal distribution and evolution of the total column of carbon monoxide (TCO) obtained from IASI observations from 1 December 2019 to 31 January 2020 are presented in Figure 2. The latitude-time Hovmöller diagram is averaged for all longitudes covering the Australian continent (between 114°E and 155°E). Figure 2 shows that the TCO is relatively homogeneously distributed with latitude before 15 December 2019. Conversely, an increase in TCO (higher than 5×10^{18} molecules·cm^{-2}) at higher latitudes can be observed between 15 December 2019 and 12 January 2020. The intensification of the CO emission is observed during the period aforementioned. The highest TCO

values, with zonal mean values exceeding 7 × 10^{18} molecules·cm^{-2}, are observed over the southern region between 29 December 2019 and 12 January 2020. This is consistent with previous studies which suggested that significant biomass burning emission may originate in Australia's temperate forests, which are located in the southern region [89,90]. The TCO values decrease (less than 3.5 × 10^{18} molecules·cm^{-2}) over all the latitude band after 12 January 2020. Nevertheless, moderate values (4–4.5 × 10^{18} molecules·cm^{-2}) are observed over the 35°S–38°S latitudinal band on 14–16 and 25–26 January 2020 (Figure 2).

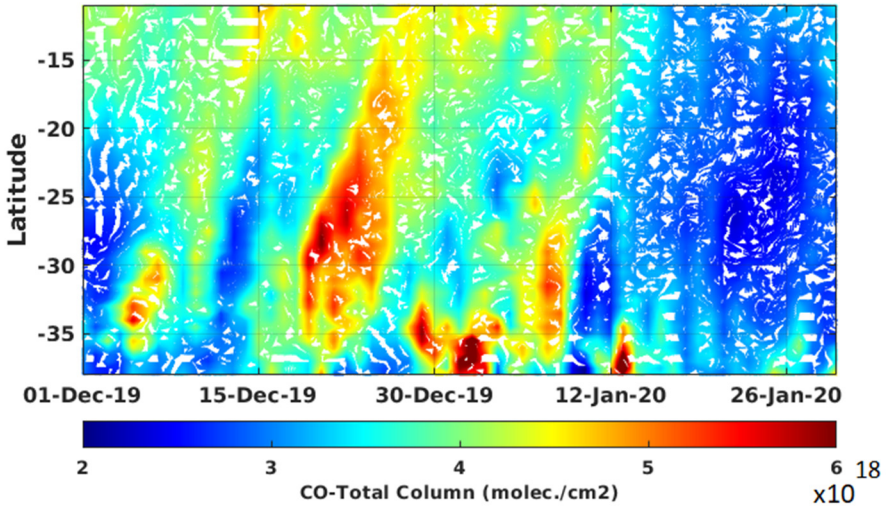

Figure 2. Hovmöller diagram of the total column of CO obtained from IASI observations over the area of Australia (between 114°E and 155°E) from 1 December 2019 to 31 January 2020.

Figure 3 depicts the daily mean evolution of AOD at 532 nm obtained from sun-photometer and CALIOP observations at six Australian sites, between 1 December 2019 and 31 January 2020 (locations displayed on Figure 1). CALIOP AOD data were collected over an area of 5° × 5° latitude × longitude centered on each selected site. The daily AOD measurements performed between 1 December 2019 and 31 January 2020 were compared to background values (2010–2018) obtained from sun-photometer observations. Background values of AOD decrease with increasing latitude, which is consistent with previous studies [91,92]. Sun-photometer and CALIOP measurements are complementary and, together, show full temporal evolution of the AOD over each site. This is clearly illustrated with the case of the Tumbarumba site, where no measurements were recorded by the sun-photometer after 4 January 2020 (Figure 3f). It is worth noting that the AOD evolution obtained from CALIOP and sun-photometer are in fairly good agreement over all sites. This confirms that the high AOD values (higher than background values) over southern sites (such as Fowlers Gap and Tumbarumba) did not result from a technical artefact, but were observed by multiple independent instruments. Figure 3 reveals that the daily evolutions of the AOD obtained from sun-photometer and CALIOP over all the selected sites show significant increases (higher than background values) between 15 December 2019 and 12 January 2020. These AOD anomalies appear to increase southward with higher latitude. This is similar to the latitudinal distributions obtained for TCO presented in Figure 2.

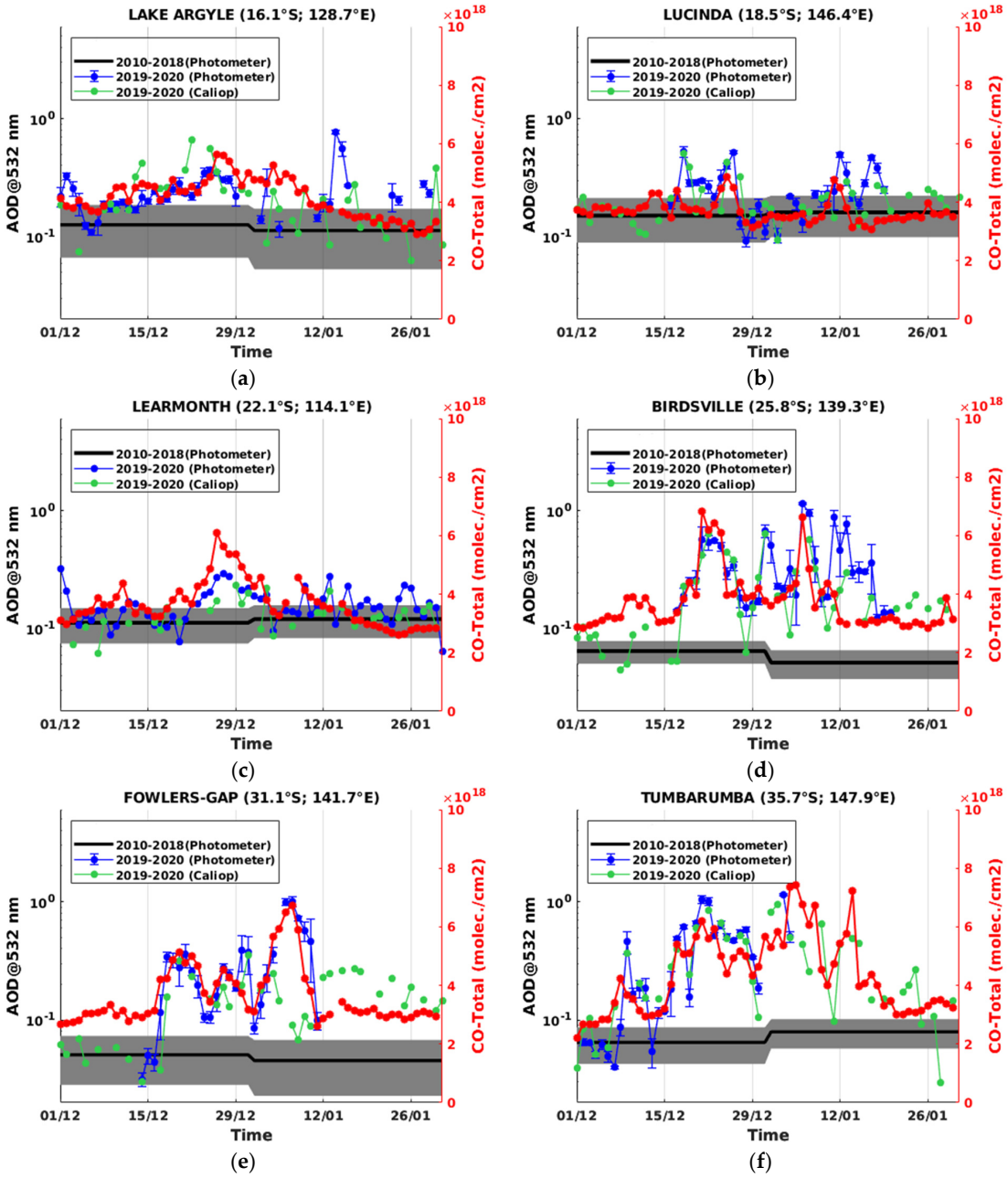

Figure 3. Daily mean of AOD (532 nm) obtained from sun-photometer (blue dots) and CALIOP (green dots, collected over an area of 5° × 5° latitude × longitude centered on each site) observations over the (**a**) Lake Argyle, (**b**) Lucinda, (**c**) Learmonth, (**d**) Birdsville, (**e**) Fowlers Gap and (**f**) Tumbarumba sites from 1 December 2019 to 31 January 2020. The AOD monthly mean and the associated standard deviation calculated during the 2010–2018 period are in black line and grey area, respectively. The red line corresponds to daily mean of total column of CO from IASI.

Figure 3 depicts also the daily mean evolutions of TCO (in red lines) obtained from IASI observations over all sites from 1 December 2019 to 31 January 2020. It can be observed that the daily TCO and AOD evolutions during the aforementioned period are strongly correlated over all sites. This suggests that the significant increase in daily AOD values between 15 December and 12 January 2020 is most likely due to the biomass burning activity. Due to its geographical location, the Tumbarumba site is clearly the most exposed to intense fires (Figure 1). As a result, the highest differences between daily measurements and the background values are observed over this site (on average with a factor greater than 3, Figure 3f). Conversely, the lowest differences with the background values (on

average with a factor less than 2.5) are observed over the northern sites (Figure 3a–c). As discussed previously, the fires over northern Australia were less intense than the fires located over southeastern Australia. A surprising result may be the influence of the biomass burning activity on the evolution of AOD between 15 December 2019 and 12 January 2020 over Birdsville and Fowlers Gap. These two sites are far away from the fire areas, which are mainly located on the Australian coast (Figure 1). Furthermore, Birdsville and Fowlers Gap are located near Australia's major dust sources [90–92]. Mukkavilli et al. [92] revealed that dust is the major type of atmospheric aerosol over central Australia. Nevertheless, we cannot exclude the hypothesis that the significant increase in AOD and TCO over Birdsville and Fowlers Gap is a result of regional transport of biomass burning aerosols and CO from eastern and southeastern Australia. By the use of the HYSPLIT back-trajectory model and sun-photometer observations, Qin and Mitchell [91] found that smoke generated from fires in eastern and southeastern Australia can be transported across New South Wales to central Australia. Yang et al. [93] performed a cluster analysis on simulated HYSPLIT back-trajectories during the biomass burning seasons from 2005 and 2020 at ground level in Australia. They found that 32% of air masses over central Australia come from southeastern Australia during the biomass burning period. Based on CALIOP observations and the HYSPLIT model, Yang et al. [73] found that aerosols from southeastern Australia were transported toward Birdsville during the 18–26 December 2019 period from ground level to 5 km above sea level. The air masses loaded with aerosols and CO can thus be transported to central Australia.

In summary, the recirculation of air masses from southeastern to central Australia is a dynamical scheme frequently observed during the biomass burning period [90,91,93]. This dynamical scheme is characterized by a high-pressure level system developed over the eastern side and a cold front over the southwestern side. The two systems moved eastward, which led to northwesterly flow over southeastern Australia. The cold front acted as a physical barrier and brought warm dry air mass into a small corridor stretched from southeastern Australia toward the Tasman sea [31]. Therefore, this dynamical scheme is responsible for the spatial and temporal distributions of aerosols and chemical species such as CO within Australia, and also the transport of the plume towards the ocean.

3.2. Tropospheric Smoke Plume

Air masses loaded with aerosols and chemical species are frequently transported toward the Tasman Sea during the biomass burning period [28,32]. Figure 4 depicts the daily averaged maps of TCO and AAI over Oceania between 31 December 2019 and 2 January 2020. One can observe the strong correlation in the shape and spatio-temporal distributions between CO and absorbing aerosol plumes. Therefore, it can be deduced that the absorbing aerosols observed over the Oceania region can be broadly attributed to the Australian biomass burning event. The most intense transport event of Australian smoke plume occurred during the aforementioned period with large values of TCO (higher than 9×10^{18} molecule·cm^{-2}) and AAI (higher than 12) observed over the Oceania region. The CO and absorbing aerosol plumes were transported by the northwesterly flow over the Tasman Sea and reached New Zealand during New Year's Eve (Figure 4a,b). On 31 December 2019, the southern part of New Zealand was significantly impacted by the Australian biomass burning emissions with TCO and AAI values equal to 10×10^{18} molecule·cm^{-2} and 14, respectively. The TCO and AAI observations indicate that the main part of the biomass burning plume moved northeast of New Zealand on 1 January 2020 (Figure 4c,d). The biomass burning plume moved further east and was located over the Pacific Ocean on 2 January 2020 (Figure 4e,f). These large values of AAI (12–14) are consistent with the AOD values greater than 5 obtained from TROPOMI observations over the east of New Zealand on 2 January 2020 [94].

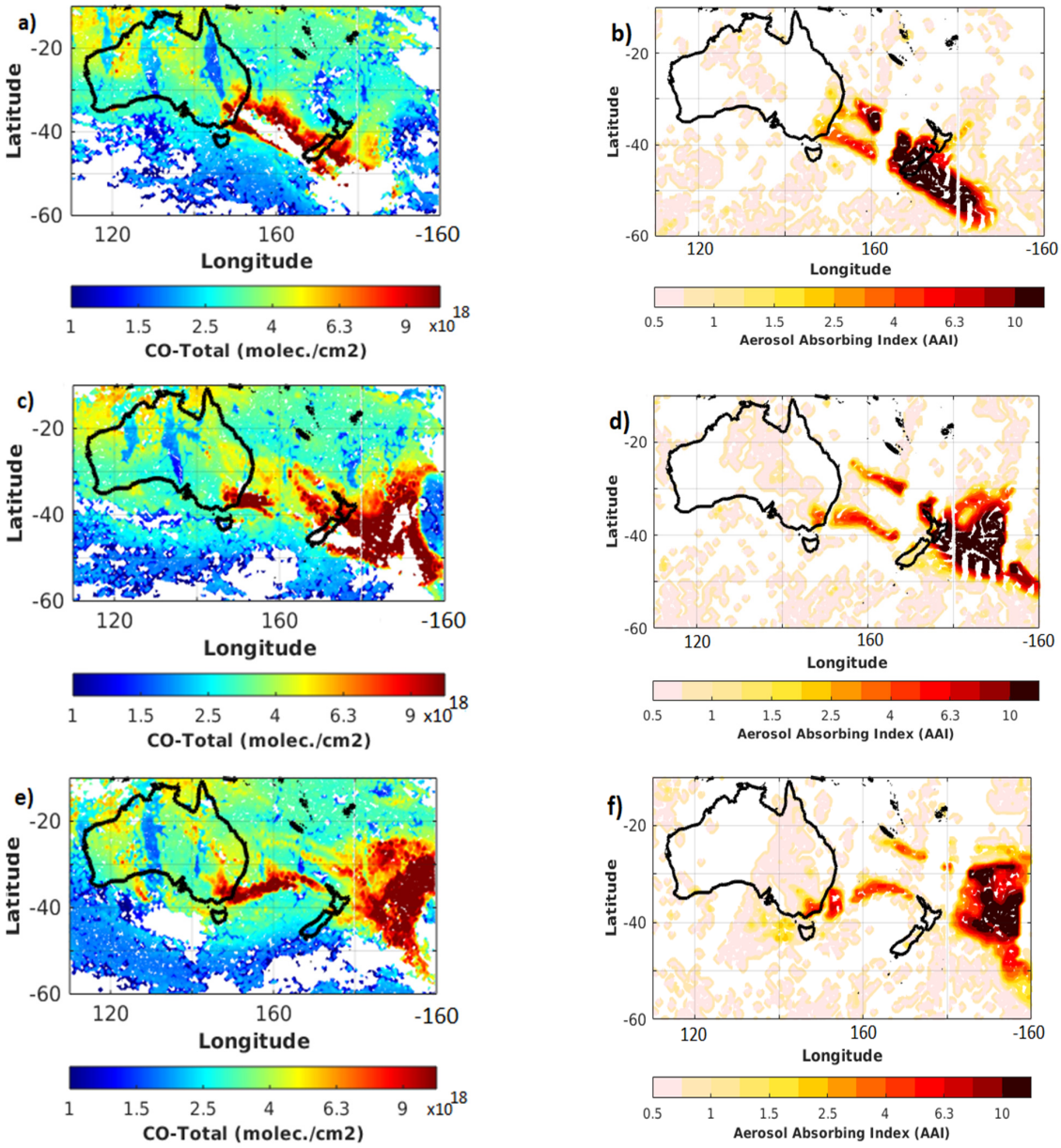

Figure 4. Daily maps of CO total columns (**a**,**c**,**e**) obtained from IASI observations and AAI (**b**,**d**,**f**) from GOME-2 observations recorded on the 31 December 2019 (top), 1 January 2020 (middle) and 2 January 2020 (bottom).

The analysis of the daily averaged map of TCO from IASI observations (such as those depicted in Figure 4) allowed us to identify five transport events of Australian CO plume passing over the Lauder site in New Zealand between 22 December 2019 and 31 January 2020 (grey shading area in Figure 5). The characteristics of these transport events are reported in Table 1. Figure 5a depicts the daily mean evolution of the TCO anomalies and total column of ozone obtained from FTIR spectrometer at Lauder during the aforementioned period. The daily anomalies induced by the transport of the Australian biomass burning plume are calculated as a relative difference by considering the standard deviation of the monthly background means as the reference values. It is worth noting that the TCO anomalies obtained from ground-based measurements are observed during the transport events of Australian CO plumes detected from IASI observations (Figure 4a). This correlation between two independent instruments corroborates the fact that the passage of the biomass burning plume induced an increase in TCO with the maximum observed on 31 December 2019 and 16 January 2020. Conversely, the passage of the plume does not

induce a systematic perturbation on the total column of ozone. It can be observed that the daily values of the total column of ozone are mainly contained inside the standard deviation of the monthly background means except for the 2–11 January 2020 period (Figure 5a). The transport of the biomass burning plume during the 2–11 January 2020 period led to concomitant increase in the CO and ozone total column.

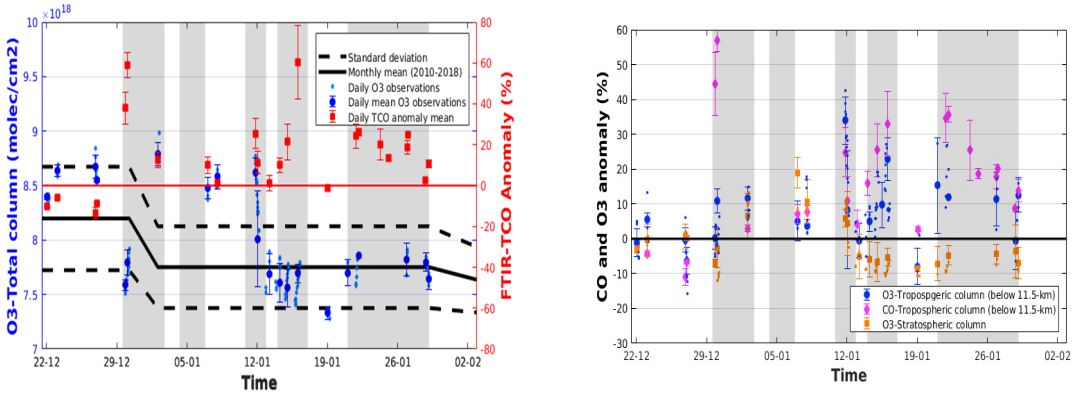

Figure 5. Daily mean evolution of total and partial column of ozone and CO obtained from FTIR observations at Lauder between 22 December 2019 and 31 January 2020. (**a**) Total column of ozone and the anomaly of total column of CO are given in the left panel, while (**b**) the anomaly of ozone (tropospheric and stratospheric) and tropospheric CO are in the right panel. The black and dash lines correspond to ozone monthly mean and the associated standard deviation calculated during the 2010–2018 period. The transport events of the Australian smoke plume detected by IASI are in the grey area.

Table 1. Characteristics of the smoke plumes sampled during their transport over Lauder. These characteristics are obtained from FTIR measurements recorded between 22 December 2019 and 31 January 2020. No measurements were recorded during the transport event #2. The period refers to time which the smoke plume is visible over Lauder from IASI observations.

Number	Period	Enriched Ozone Layer (km)	Mean $\Delta O_3/\Delta CO$ (ppbv/ppbv)	Plume Age Category
1	30 December 2019–2 January 2020	2–5	0.13 ± 0.01	≤1–2 days
2	4–6 January 2020			
3	10–12 January 2020	3–8	0.14 ± 0.05	≤1–2 days
4	15–18 January 2020	2–6	0.41 ± 0.25	2–5 days
5	20–28 January 2020	2–8	0.35 ± 0.10	2–5 days

The tropospheric and stratospheric columns of ozone were calculated from the FTIR observations at Lauder. The tropopause height was retrieved from radiosonde observations by the use of the thermal definition which is based on the lapse rate criterion [95]. The tropopause height was found on average at 11.5 ± 0.5 km during the 2019–20 austral summer months (December to February) at Lauder. We note that this value is in agreement with previous works [61,96,97]. Figure 6b depicts the evolution of the anomalies of the tropospheric and stratospheric columns of ozone at Lauder between 22 December 2019 and 31 January 2020. The anomalies were calculated by following the methodology mentioned previously. The concomitance between the tropospheric ozone anomalies and the Australian fire CO plume inferred from IASI observations are clearly shown. These transport events are, hence, marked by an increase in tropospheric ozone column with the maximum (44%) observed on 16 January 2020. Figure 5b also reveals that the tropospheric ozone anomalies are fairly correlated with the tropospheric CO anomalies. It can be observed that the stratospheric column of ozone is not significantly perturbed by the transport events. This could be explained by the temporal evolution of the tropopause height. A statistically significant increase in ozone (8%–15%) in the stratosphere is only observed during the

2–11 January 2020 period. The tropospheric ozone anomalies induced by the transport of the Australian biomass burning plume are, hence, higher than those observed in the stratospheric column.

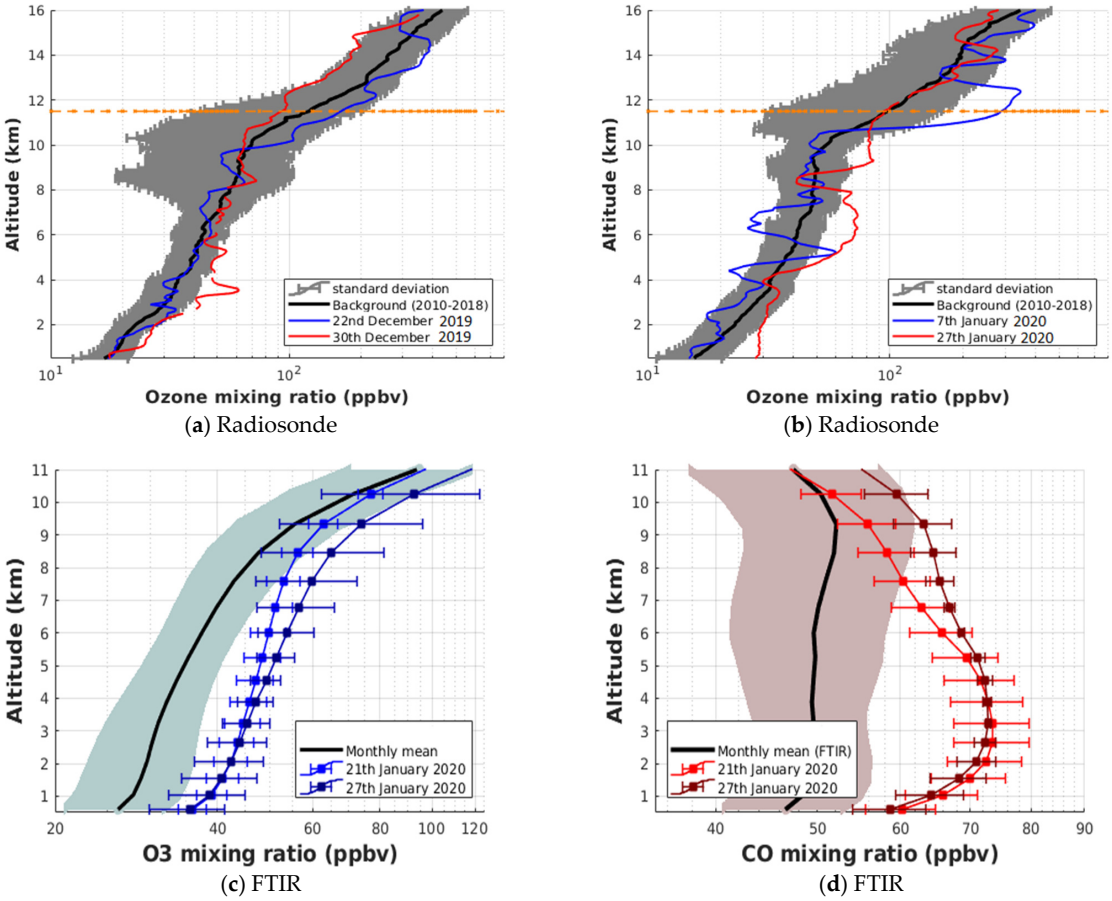

Figure 6. Available (**a**–**c**) ozone and (**d**) CO mixing ratio profiles obtained from ozone radiosondes and FTIR measurements at Lauder between December 2019 and January 2020. The monthly mean profile and the associated standard deviation calculated during the 2010–2018 period are in black line and shaded area, respectively. The tropopause height is indicated by the orange horizontal line.

Figure 6a,b depict the available OMR profiles obtained from radiosonde observations performed at Lauder during the transport events of the Australian CO plume. On 30 December 2019, the ozone profile exhibits a significant increase (16%) in the OMR between 2 and 4 km altitude (Figure 6a). The daily ozone profile falls inside the standard deviation of the monthly background profile when a "no plume" is transported over Lauder, as illustrated on 22 December 2019 (Figure 6a). Figure 6b reveals a steep concentration increase (60%) in the local UT-LS (10.5–12.5 km) on 7 January 2020. This corroborates the concomitant increase in the tropospheric and stratospheric ozone columns obtained from FTIR observations during the 2–11 January 2020 period (Figure 5b). The radiosonde measurements also confirm that the ozone contained in the stratosphere was perturbed only by the transport of the biomass burning plume that occurred during this period. Previous works have shown that the pyro-convective activity has also contributed to inject biomass burning gases such as CO and water vapor into the stratosphere [35,36]. Based on the MLS observations, Khaykin et al. [36] showed that the stratospheric mass of CO bounded within the southern extra-tropics increased abruptly by about 20% compared to the value observed before the event. The OMR anomalies are also observed during the period following the pyro-convective outbreaks, as observed on 27 January 2020 (Figure 6b). On this day, the OMR profile is marked by a significant increase (23%) located between 5 and 7.5 km

altitude. It is worth noting that the air mass back-trajectory calculations performed with the on-line HYSPLIT model (not shown) confirm the link between these ozone concentration anomalies and the Australian biomass burning activity. Given the high temporal resolution of the FTIR observations, daily analysis of the tropospheric ozone and CO mixing ratios is possible during the period of the transport events. This is illustrated with Figure 6c,d, which report the tropospheric ozone and CO mixing ratio profiles, respectively, during the 21–27 January 2020 period. Figure 6c confirms a significant increase in the OMR (25–30%) between 3 and 8 km altitude on 21 and 27 January 2020. This is fairly consistent with the ozone radiosonde observations performed on 27 January 2020 (Figure 6b). Figure 6d reveals that the OMR increase occurred in parallel with the CO mixing ratio increase within the same altitude range. The concomitant increase in ozone and CO in the troposphere suggests the production of ozone in the tropospheric smoke plume. Several studies have clearly shown that CO is an ozone precursor [98,99]. Nevertheless, it is worth noting that biomass burning plumes are chemically reactive, producing ozone and aerosols also through NO_x-VOC chemistry [100,101]. Baylon et al. [100] showed that the degree of NO_x oxidation is a key predictor of ozone production. On average, an enriched ozone layer is identifiable in the altitude range of 2–8 km, outside the pyro-convective outbreaks period (Table 1).

To further discuss the production of ozone in the tropospheric smoke plume, the $\Delta O_3/\Delta CO$ enhancement ratio was estimated for different transport events. This ratio is defined as the excess OMR above background ozone in air mass normalized by an enhancement in CO mixing ratio above background value. The $\Delta O_3/\Delta CO$ enhancement ratio is often used as a measure of ozone production efficiency in fire plume [102–104]. The $\Delta O_3/\Delta CO$ enhancement ratio values obtained for the transport events are reported in Table 1. The values obtained for the transport events detected between 30 December 2019 and 12 January 2020 are less than 0.15 ppbv/ppbv. Previous works showed that the $\Delta O_3/\Delta CO$ enhancement ratio is strongly influenced by the travel time between the fire and the measurement location [105,106]. Hence, it is possible to obtain an estimation of the plume age. The values obtained during the aforementioned transport events correspond to a plume age of less than 2 days for the tropical and subtropical regions [105,106]. Conversely, the $\Delta O_3/\Delta CO$ enhancement ratio values obtained for the two transport events detected after 13 January 2020 are higher than 0.2 ppbv/ppbv. Table 1 reveals that the ratio values obtained during the transport events #3 and #4 are 0.41 ± 0.25 ppbv/ppbv and 0.35 ± 0.10 ppbv/ppbv, respectively. These values correspond to a plume age between 2 and 5 days for the tropical and subtropical regions [105,107]. The plumes sampled during these transport events are, hence, relatively freshly emitted (between 1 and 5 days) from fires located over Australia.

The transport of Australian biomass burning plume led to significant perturbation of the chemical composition in the troposphere over Lauder and its surroundings. It is clearly shown that ozone has been produced in the tropospheric smoke plume. This corroborates the results found by Baray et al. [108]. Based on radiosonde observations and back-trajectory modeling, they showed that the tropospheric ozone variability at Lauder is influenced by biomass burning plumes emitted from Australian fires during the austral summer months. In order to extend the discussion, the dispersion of the tropospheric ozone plume will be analyzed in the next section.

4. Discussion on the Tropospheric Ozone Variability

4.1. Spatial Extend of the Tropospheric Ozone Plume

Figure 7 shows maps of IASI TCO and tropospheric ozone column averaged over three successive periods: 18–20 December 2019, 4–5 January and 8–11 January 2020. These periods are associated with the phase of intensification of CO emission over southeastern and eastern Australia (Section 3). A fairly good agreement in the shape and the spatio-temporal distributions between the TCO and tropospheric ozone column is observed. Thus, it can be inferred that the tropospheric ozone variability was mainly driven by the Australian smoke

plume. On 18–20 December 2019, the highest values of TCO (6.3×10^{18} molecules·cm^{-2}) and tropospheric ozone column (65–70 DU) are found over the eastern Australia coast (Figure 7a,b). Samoa is located at the edge of the CO plume (4–4.5×10^{18} molecule·cm^{-2}). The tropospheric ozone column values observed over Samoa range from 40 to 50 DU. Despite the fact that Amazonian biomass burning activity is usually sparse in December and January, moderate values of TCO (4–5×10^{18} molecules·cm^{-2}) and tropospheric ozone column (30–40 DU) are observed over South America (Figure 7a,b). MODIS fire products (not shown) confirm the coincidence with these moderate CO and tropospheric ozone column values areas and fire pixels over South America, by showing a few biomass burning events less intense than those observed during the Amazonian biomass burning season. Part of the ozone and the CO produced by these fires are usually transported toward the eastern Pacific [43,108]. This explains the moderate values of CO and tropospheric ozone column observed over the northwestern coast of South America and its surroundings. Hence, we can exclude any association between the moderate values of CO and tropospheric ozone column over the aforementioned region and the Australian biomass burning activity at this period of time. The analysis of the IASI observations revealed that the transport of the Australian smoke plume occurring out of the pyro-cumulus outbreak period did not cross the Southern Pacific. Up until 29 December 2019, the smoke plumes were transported mainly over the Oceania region by following fairly pathways similar to those in Figure 7a,b. The smoke plumes were mainly transported to the north of New Zealand within subtropical and tropical latitudinal bands in the days before the pyro-cumulonimbus outbreaks period (Figure 7a,b).

In the days following the pyro-cumulonimbus events, the smoke plumes were transported toward Southern Pacific, as is illustrated in Figures 4 and 7c. This could be explained by the fact that the pyro-convection events can quickly lift aerosol and chemical species to the UT-LS region, leading to changes in its composition [28]. Figure 7c reveals that the CO plume (from 6.3×10^{18} to 9×10^{18} molecules·cm^{-2}) crossed the Southern Pacific by passing over New-Zealand during the 4–5 January 2020 period. The tropospheric ozone column values associated with the transport of the Australian biomass burning plume over the Southern Pacific ranged from 60 to 70 DU during the aforementioned period (Figure 7d). On 4–5 January 2020, the CO and tropospheric ozone plumes were close to the tip of South America. This corroborates the observations reported by Ohneiser et al. [37] at Punta Arena (53.2°S, 70.9°E; Chile). By using LIDAR measurements at Punta Arena, they showed that the smoke layer was visible over Punta Arena since 6 January 2020 in the upper troposphere (between 6 and 11 km altitude) and has fallen gradually over time. The tropospheric plume was driven rapidly by the westerly winds and finally dissipated over the Atlantic Ocean. On 8–10 January 2020, the CO plume is centered over the Southern Pacific and is organized following an anti-cyclonic rolling extending between 20°S and 40°S (Figure 7e). The plume's structure in Figure 7e can be associated with the anticyclonic rolling of the CO plume. This is consistent with the work reported by Khaykin et al. [36]. They showed that on its way across the Southern Pacific during the first week of 2020, the core plume started to encapsulate into a compact bubble-like structure. This was identified in CALIOP observations on 7 January 2020 as an isolated 4 km vertically extended and 1000 km horizontally wide structure. The IASI observations reveal that the CO plume, by its rolling and stretching, has extended the tropical and subtropical latitudinal bands during the 8–14 January 2020 period. Figure 7f shows that the tropospheric ozone plume is also centered over the Southern Pacific between 20°S and 40°S with values ranging from 40 to 50 DU. The tropospheric ozone plume is not clearly organized following the anti-cyclonic rolling structure in Figure 7f. The structure of the tropospheric ozone plume is more diffuse and extends over the Samoan measurement site (Figure 7f). Furthermore, it was observed that plumes of CO and tropospheric ozone have spread further into the extra-tropical latitudes after 14 January 2020, crossing the southwestern part of South America one day later. Previous works confirm that South America is frequently impacted by the Australian biomass burning plume during the pyro-convective activity [28,33]. Through the use of

OMI RGB images and AAI observations, Dirksen et al. [28] showed that the 2006 Australian bushfire smoke plumes were transported eastward and traveled from Tasmania to Chile within five days.

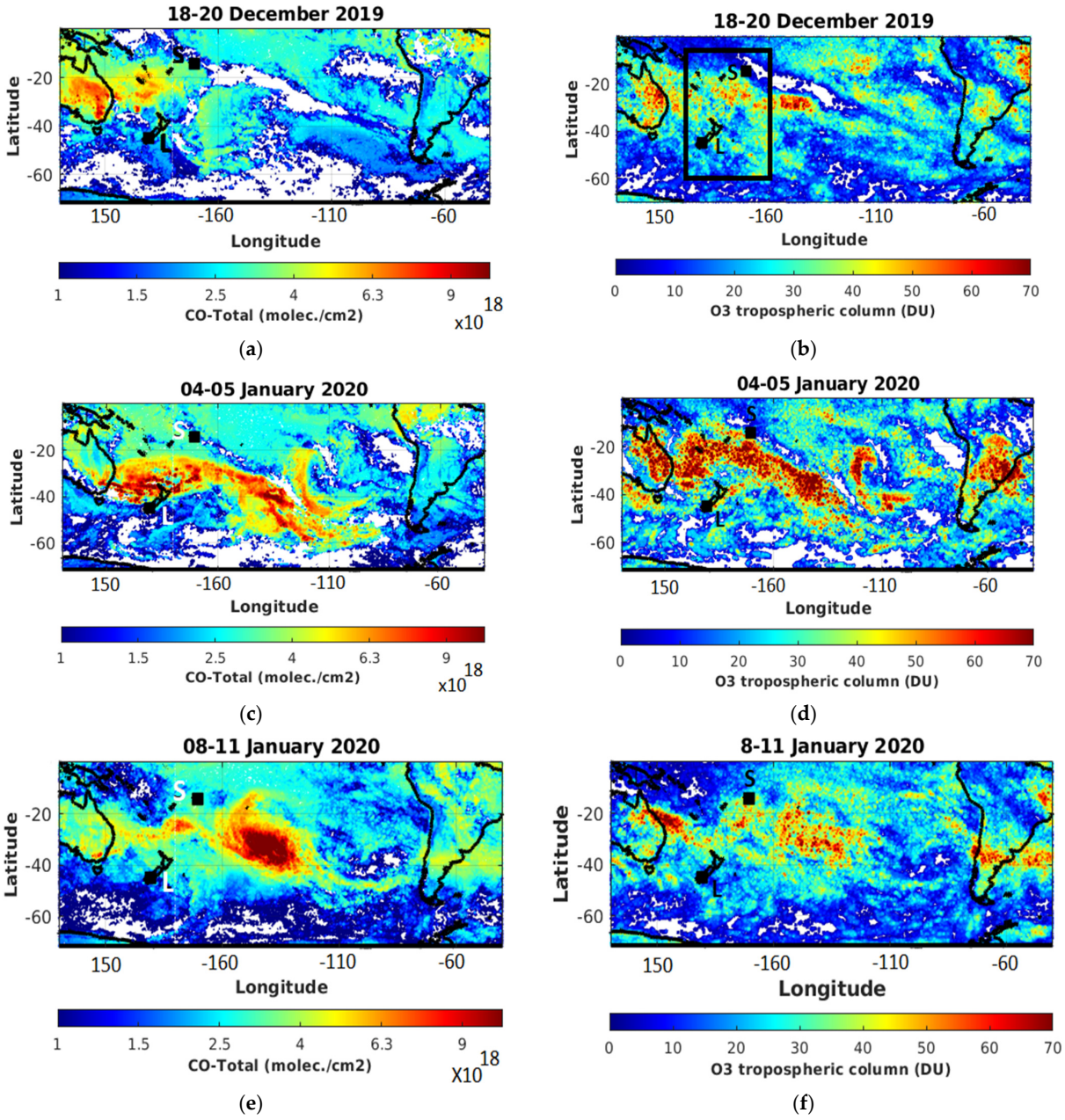

Figure 7. Time-averaged map of (left panel) total column of CO and (right panel) tropospheric ozone column obtained from IASI observations averaged over three successive periods, i.e., (**a**,**b**) on 18–20 December 2019, (**c**,**d**) on 4–5 January and (**e**,**f**) on 8–11 January. The location of the Samoa and Lauder sites are indicated by black boxes and the abbreviation sites (S for Samoa and L for Lauder).

In addition to local tropospheric ozone sources from northern parts of South America, the Australian biomass burning plumes contributed, hence, to tropospheric ozone column variability over the southern part of South America, as is illustrated in Figure 7.

4.2. Statistical Variation of the Tropospheric Ozone

Given the presence of local tropospheric ozone sources, it is difficult to estimate properly the contribution of the Australian biomass burning activity to the tropospheric

ozone variability over Southern America from space-borne observations. As a consequence, the discussion focuses on tropospheric ozone variability over Oceania. It can be observed that the transport of the Australian biomass burning plume over Oceania occurred mainly within the 18°S–60°S latitudinal band (Figure 7). To further investigate the latitudinal ozone variability induced by the transport of the Australian biomass burning plume over the Oceania region, the daily mean evolution of the OMR obtained from MLS observations between 18 December 2019 and 31 January 2020 was calculated over a global domain extending between 10°S and 60°S in latitude and 160°E and 160°W in longitude (the black box in Figure 7b) at 215 (~12 km) and 100 hPa (~16 km) levels (Figure 8). The ozone anomalies at 215 hPa are mainly observed during the two first weeks of January for the three latitudinal bands: tropical (10°S–19°S), subtropical (20°S–29°S) and extratropical (30°S–60°S). Over the extratropical latitudinal band, the maxima of OMR anomalies (from 12% to 47%) were obtained during the 2–8 January 2020 period (Figure 8e). This suggests that ozone mixed vertically by convection over southeastern and eastern Australia and was then transported toward this latitude band in the UT-LS. Conversely, the maxima of the OMR anomalies (from 5% to19%) is observed during the 6–12 January 2020 period over the tropical latitudinal band (Figure 8c). This could be explained by the presence of the large and stretchable ozone plume over the Southern Pacific during the aforementioned period. Given its geographical extension, we cannot exclude that this large ozone plume led to sporadic ozone anomalies within the tropical and subtropical latitudinal bands over Oceania. It is worth noting that the daily evolution of the OMR does not exhibit statistically significant perturbation at 100 hPa over the tropical latitudinal band (Figure 8b). Conversely, the daily evolution of the OMR exhibits statistically significant perturbation over extratropical and subtropical latitudinal bands, with the maximum observed over the latter (Figure 8d,f). The IASI observations (Figures 4 and 7) reveal that parts of the smoke plume are contained within the subtropical latitudinal bands during the pyro-cumulonimbus outbreaks. The large and stretchable ozone plume over the Southern Pacific had the potential to induce ozone anomalies within the Oceanian subtropical band. In OMR evolution at 215 and 100 hPa over the subtropical latitudinal band, there is a statistically significant increase in ozone (from 19% to 46%) during the 1–14 January 2020 period (Figure 8c,d).

Figure 9a,b depict the available OMR profiles obtained from radiosonde observations recorded at Samoa between 18 December 2019 and 15 January 2020. The ozone profile exhibits a significant increase (43%) in the OMR between 6 and 9 km altitude, on 18 December 2019 (Figure 9a). Figure 7a,b corroborate that this enhanced ozone layer is linked to the transport of Australian biomass burning plume that occurred between 18 and 20 December 2019. Given the reasons previously mentioned and collaborating satellite observations, we can exclude all contributions from Southern African and Indonesian sources on the enhanced ozone seen in the mid-troposphere on 18 December 2019. The enhancement lasted for only a few days. On 26 December 2019, the daily ozone profile falls inside the standard deviation of the monthly background profile (Figure 9a). It can be observed that the OMR profile recorded at Samoa exhibits two distinct enhanced ozone layers centered in the mid (6–9 km) and upper troposphere (10–12 km), on 8 January 2020 (Figure 9b). These two enhanced ozone layers do not appear to be connected to each other. The origin of the enhanced ozone layer into the mid-troposphere is similar to the one observed on 18 December 2019. Figure 7f shows that the transport of the tropospheric ozone plume towards the Tasman Sea was located over Northeastern Australia during the 8–10 January 2020 period. This biomass burning plume has contributed to a significant increase (from 10% to 43%) in OMR over Samoa (Figure 7f). We cannot exclude that the presence of this large and stretchable ozone plume has led to a significant increase (29%) in OMR at Samoa between 10 and 12 km. We suspect that this ozone profile recorded in Samoa resulted from air-mass crossing in the local mid-troposphere, from eastern Australia and the Western Pacific. On 15 January 2020, it can be observed that the daily ozone profile falls inside the standard deviation of the monthly background profile climatology. On 15 January 2020,

it can be observed that the daily ozone profile falls inside the standard deviation of the monthly background profile. This could be explained by the fact that the biomass burning plume was preferentially transported toward extratropical latitudes since 14 January 2020. As a consequence, the tropical sites such as Samoa are less impacted by the biomass burning plume. It is worth noting that a similar increase in the OMR was obtained at Lauder and Samoa. For both sites, the enhanced ozone layers due to the transport of the Australian biomass burning are in the mid- and upper-troposphere. Overall, we conclude that the transport of the smoke plume into the troposphere was not bounded exclusively within the extratropical latitudinal band.

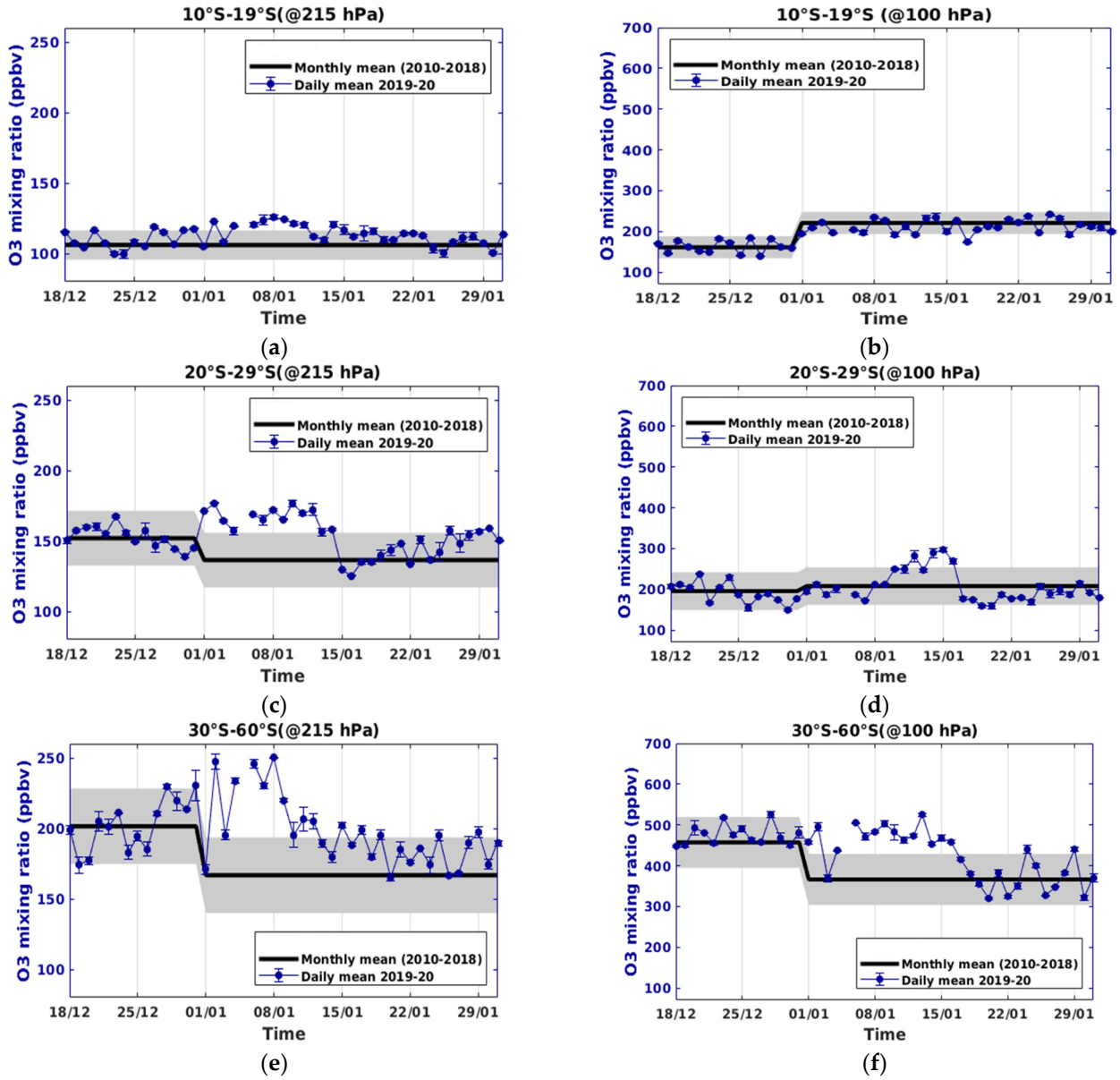

Figure 8. Daily mean evolution of the latitudinal mean of OMR (blue lines) obtained from MLS at 215 hPa (**a**,**c**,**e**) and 100 hPa (**b**,**d**,**f**) between 18 December and 31 January 2020 over Oceania (black box in Figure 7b). The OMR mean values are calculated over tropical (top, 10°S–19°S), subtropical (middle, 20°S–29°S) and extratropical (bottom, 30°S–60°S) latitudinal bands. The monthly mean and the associated standard deviation calculated over the 2010–2018 period are in black lines and grey areas, respectively.

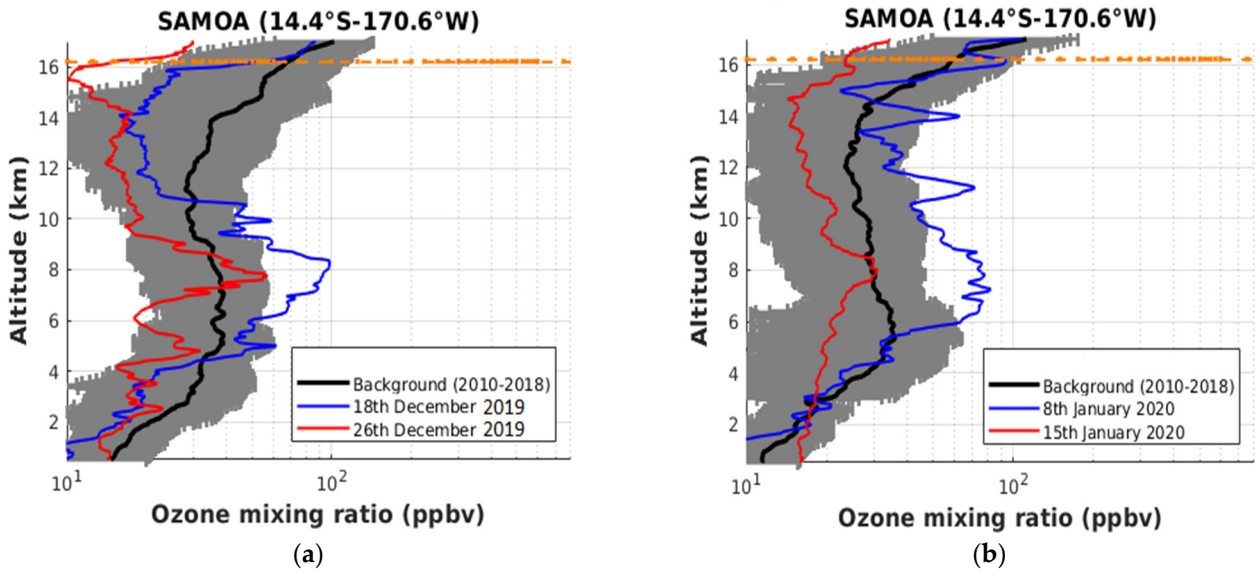

Figure 9. OMR profiles obtained from ozone radiosonde measurements performed at Samoa on (**a**) December 2019 and (**b**) January 2020. The monthly mean profile and the associated standard deviation calculated during the 2010–2018 period are in black lines and grey areas, respectively. The tropopause height is indicated by the orange horizontal lines.

5. Conclusions

We presented the tropospheric ozone and CO variability over Oceania and the Southern Pacific during the 2019–20 Australian bushfires. The meteorological context and the extensive fires over southeastern Australia were favorable to develop pyro-cumulonimbus events between 29 December and 12 January 2020. The latitudinal variation of the TCO over Australia obtained from IASI was found to be consistent with the latitudinal distribution of the AOD. The sun-photometer and CALIOP observations showed that the highest values of AOD were found between 15 December 2019 and 12 January 2020 over southern and central Australia. The spatial and temporal distributions of aerosol and CO over Australia are mainly explained by the recirculation of air masses from the southeastern to central region of the continent.

The analysis of the satellite observations revealed that transport events of Australian biomass burning plume took place during and outside of the pyro-cumulonimbus outbreak period. The dispersion of the smoke plume during these transport events extends from tropical to extratropical latitudes. The dispersion of these smoke plumes induced a significant variability on the tropospheric ozone column detected from satellite and FTIR observations. The ozone radiosonde measurements performed at Samoa and Lauder recorded enhanced ozone layers in the mid-tropospheric ozone linked with transport events of the Australian biomass burning plumes. This increase in ozone in the mid-troposphere was found to be consistent with MLS observations over the tropical and extratropical latitudinal bands. The smoke plume was transported over the Southern Pacific. The IASI observations confirm that smoke plume transport over the Southern Pacific had led to significant ozone variability in the troposphere. The smoke plume remained over the Southern Pacific for a few days before moving into the extra-tropics and reaching the southwestern part of South America. Over the southern Pacific, the smoke plume was organized following a stretchable anticyclonic rolling which impacted significantly on the ozone variability in the tropical and subtropical upper-troposphere over Oceania.

Our analysis suggests that these transport events of Australian biomass burning plumes significantly alter the chemical composition in the troposphere over Oceania and the Southern Pacific. Besides the injection of aerosol particles and chemical species into the stratosphere, the dynamical context has also contributed to modify the vertical distribution of aerosol and chemical species such as ozone in the troposphere at the regional scale. To understand the full contribution of the extreme Australian bushfire events to the tropo-

spheric distribution of aerosol and chemical species, further investigation is required by including numerical models (such as WRF-Chem) with fire pollution sources. The dataset presented in this study would be useful to validate and constrain the numerical simulations. Given similar dynamical context was observed during previous extreme Australian bushfire events [28,31,109], it cannot be excluded that perturbations on tropospheric trace gas abundances were also observed during these events. The potential of these previous extreme bushfire events to induce significant perturbation on the tropospheric distribution of aerosol and chemical species over Australia and its surroundings will form the basis for a forthcoming statistical study.

Author Contributions: Conceptualization, N.B.; methodology and software, N.B, H.B., F.J., H.V. and G.K.; validation and data curation, N.B., H.B., F.J., H.V., V.D., C.C., P.-F.C., D.S., J.R., R.Q. and P.S.; original draft preparation and writing, N.B.; review and editing, C.K., G.P., N.B., H.B., H.V., F.J., G.B., P.K., V.D., T.P., A.B., S.K., D.S. and C.C.; project administration and funding acquisition, N.B. All authors have read and agreed to the published version of the manuscript.

Funding: This research received no external funding.

Institutional Review Board Statement: Not applicable.

Informed Consent Statement: Not applicable.

Data Availability Statement: The aerosols and trace gases measurements from ground-based (sun-photometer, radiosondes, FTIR) and satellite (MLS, CALIOP, MODIS, GOME-2, IASI) observations are available on-line from the sources as stated in the manuscript.

Acknowledgments: We thank Ian Lau, Thomas Schroder and their staff for establishing and maintaining the sun-photometer at Learmonth, Lake Argyle, Lucinda, Birdsville, Folows Gap and Tumbarumba sites used in this investigation (http://aeronet.gsfc.nasa.gov/, last access: 21 June 2021). The authors thank the NDACC (http://www.ndacc.org, last access: 21 June 2021). and SHADOZ (https://tropo.gsfc.nasa.gov/shadoz/, last access: 21 June 2021) network for providing the ozonesonde data for this study at Lauder and Samoa respectively. IASI was developed and built under the responsibility of the "Centre National d'Etudes Spatiales" (CNES, France). It is flown on board the MetOp satellites as part of the EUMETSAT Polar System. The authors thank the AERIS infrastructure (https://iasi.aeris-data.fr/, last access: 27 July 2021) for providing access to the IASI data, the National Aeronautical and Space Administration (NASA) for providing CALIOP data and MODIS fire products. The FTIR data were providing by the NDACC network. The NIWA Lauder measurements are supported by the New Zealand Ministry of Business, Innovation and Employment (MBIE) Strategic Science Investment Fund (SSIF).

Conflicts of Interest: The authors declare no conflict of interest.

References

1. Krupa, S.V.; Manning, W.J. Atmospheric ozone: Formation and effects on vegetation. *Environ. Pollut.* **1988**, *50*, 101–137. [CrossRef]
2. Andreae, M.O.; Merlet, P. Emission of trace gases and aerosols from biomass burning. *Glob. Biogeochem. Cycles* **2001**, *15*, 955–966. [CrossRef]
3. Crutzen, J.P.; Carmichael, G.R. Modeling the influence of fires on atmospheric chemistry. In *Fire in the Environment: The Ecological, Atmospheric, and Climatic Importance of Vegetation Fires*; Crutzen, P.J., Goldhammer, J.G., Eds.; John Wiley: New York, NY, USA, 1993; pp. 89–106.
4. Duflot, V.; Dils, B.; Baray, J.L.; de Maziere, M.; Attié, J.-L.; Vanhaelewyn, G.; Senten, C.; Vigouroux, C.; Clain, G.; Robert, D. Analysis of the origin of the distribution of CO in the subtropical southern Indian Ocean in 2007. *J. Geophys. Res.* **2010**, *115*, D22106. [CrossRef]
5. Wang, W.; Pinto, J.P.; Yung, Y.L. Climatic effects due to halogenated compounds in the Earth's atmosphere. *J. Atmos. Sci.* **1980**, *37*, 333–338. [CrossRef]
6. Garstang, M.; Tyson, P.D.; Swap, R.; Edwards, M.; Kållberg, P.; Lindesay, J.A. Horizontal and vertical transport of air over southernAfrica. *J. Geophys. Res.* **1996**, *101*, 23721–23736. [CrossRef]
7. Holanda, B.A.; Pöhlker, M.L.; Walter, D.; Saturno, J.; Sörgel, M.; Ditas, J.; Pöhlker, C. Influx of African biomass burning aerosol during the Amazonian dry season through layered transatlantic transport of black carbon-rich smoke. *Atmos. Chem. Phys.* **2020**, *20*, 4757–4785. [CrossRef]
8. Torres, O.; Chen, Z.; Jethva, H.; Ahn, C.; Freitas, S.R.; Bhartia, P.K. OMI and MODIS observations of the anomalous 2008–2009 Southern Hemisphere biomass burning seasons. *Atmos. Chem. Phys.* **2010**, *10*, 3505–3513. [CrossRef]

9. Morgenstern, O.; Zeng, G.; Wood, S.W.; Robinson, J.; Smale, D.; Clare, M.; Jones, N.B.; Griffith, D.W.T. Long-range correlations in Fourier transform infrared, satellite, and modeled CO in the Southern Hemisphere. *J. Geophys. Res.* **2012**, *117*, D11301. [CrossRef]
10. Edwards, D.P.; Emmons, L.K.; Gille, J.C.; Chu, A.; Attié, J.L.; Giglio, L.; Drummond, J.R. Satellite-observed pollution from Southern Hemisphere biomass burning. *J. Geophys. Res.* **2006**, *111*, D14312. [CrossRef]
11. Oltmans, S.J.; Johnson, B.J.; Harris, J.M.; Vömel, H.; Thompson, A.M.; Koshy, K.; Paredes, F. Ozone in the Pacific tropical troposphere from ozonesonde observations. *J. Geophys. Res. Atmos.* **2001**, *106*, 32503–32525. [CrossRef]
12. Pak, B.; Langenfelds, R.; Young, S.; Francey, R.; Meyer, C.; Kivlighon, L.; Cooper, L.N.; Dunse, B.; Allison, C.; Steele, L.P.; et al. Measurements of biomass burning influences in the troposphere over southeast Australia during the SAFARI 2000 dry season campaign. *J. Geophys. Res.* **2003**, *108*, 8480. [CrossRef]
13. Kaiser, J.W.; Keywood, M. Preface for Atmos. Env. Special issue on IBBI. *Atmos. Environ.* **2015**, *121*, 1–3. [CrossRef]
14. Russell-Smith, J.; Yates, C.P.; Whitehead, P.J.; Smith, R.; Craig, R.; Allan, G.E.; Thackway, R.; Frakes, I.; Cridland, S.; Meyer, M.C.P.; et al. Bushfires' down under': Patterns and implications of contemporary Australian landscape burning. *Int. J. Wildland Fire* **2007**, *16*, 361–377. [CrossRef]
15. Mallet, M.D.; Desservettaz, M.J.; Miljevic, B.; Milic, A.; Ristovski, Z.D.; Alroe, J.; Cravigan, L.T.; Jayaratne, E.R.; Paton Walsh, C.; Griffith, D.W.T.; et al. Biomass burning emissions in north Australia during the early dry season: An overview of the 2014 SAFIRED campaign. *Atmos. Chem. Phys.* **2017**, *17*, 13681–13697. [CrossRef]
16. Shi, Y.; Matsunaga, T.; Saito, M.; Yamaguchi, Y.; Chen, X. Comparison of global inventories of CO_2 emissions from biomass burning during 2002–2011 derived from multiple satellite products. *Environ. Pollut.* **2015**, *206*, 479–487. [CrossRef]
17. van der Werf, G.R.; Randerson, J.T.; Giglio, L.; Collatz, G.J.; Kasibhatla, P.S.; Arellano, A.F., Jr. Interannual variability in global biomass burning emissions from 1997 to 2004. *Atmos. Chem. Phys.* **2006**, *6*, 3423–3441. [CrossRef]
18. Andersen, A.N.; Cook, G.D.; Corbett, L.K.; Douglas, M.M.; Eager, R.W.; Russell-Smith, J.; Setterfield, S.A.; Williams, R.J.; Woinarski, J.C. Fire frequency and biodiversity conservation in Australian tropical savannas: Implications from the Kapalga fire experiment. *Aust. Ecol.* **2005**, *30*, 155–167. [CrossRef]
19. Williams, R.J.; Gill, A.M.; Moore, P.H.R. Seasonal changes in fire behaviour in a tropical savanna in northern Australia. *Int. J. Wild. Fire* **1998**, *8*, 227–239. [CrossRef]
20. Ristovski, Z.D.; Wardoyo, A.Y.; Morawska, L.; Jamriska, M.; Carr, S.; Johnson, G. Biomass burning influenced particle characteristics in Northern Territory Australia based on airborne measurements. *Atmos. Res.* **2010**, *96*, 103–109. [CrossRef]
21. Cruz, M.G.; Sullivan, A.L.; Gould, J.S.; Sims, N.C.; Bannister, A.J.; Hollis, J.J.; Hurley, R.J. Anatomy of a catastrophic wildfire: The Black Saturday Kilmore East fire in Victoria Australia. *For. Ecol. Manag.* **2012**, *284*, 269–285. [CrossRef]
22. Sullivan, A.L.; McCaw, W.L.; Cruz, M.G.; Matthews, S.; Ellis, P.F. Fuel, fire weather and fire behaviour in Australian ecosystems. In *Flammable Australia*; Bradstock, R.A., Gill, A.M., Williams, R.D., Eds.; CSIRO Publishing: Collingwood, Australia, 2012.
23. Dowdy, A.J.; Pepler, A. Pyroconvection risk in Australia: Climatological changes in atmospheric stability and surface fire weather conditions. *Geophys. Res. Lett.* **2018**, *45*, 2005–2013. [CrossRef]
24. Fromm, M.; Lindsey, D.T.; Servranckx, R.; Yue, G.; Trickl, T.; Sica, R. The untold story of pyro-cumulonimbus. *Bul. Am. Meteorol. Soc.* **2010**, *91*, 1193–1210. [CrossRef]
25. Fromm, M.; Tupper, A.; Rosenfeld, D.; Servranckx, R.; McRae, R. Violent pyro-convective storm devastates Australia's capital and pollutes the stratosphere. *Geophys. Res. Lett.* **2006**, *33*, L05815. [CrossRef]
26. Mitchell, R.M.; O'Brien, D.M.; Campbell, S.K. Characteristics and radiative impact of the aerosol generated by the Canberra firestorm of January 2003. *J. Geophys. Res. Atmos.* **2006**, *111*, D02204. [CrossRef]
27. McRae, R.H.D.; Sharples, J.J.; Wilkes, S.R.; Walker, A. An Australian pyro-tornadogenesis event. *Nat. Haz.* **2013**, *65*, 1801–1811. [CrossRef]
28. Dirksen, R.J.; Boersma, K.F.; de Laat, J.; Stammes, P.; van der Werf, G.R.; Martin, M.V.; Kelder, H.M. An aerosol boomerang: Rapid around-the-world transport of smoke from the December 2006 Australian forest fires observed from space. *J. Geophys. Res.* **2009**, *114*, D21201. [CrossRef]
29. Fromm, M.D.; McRae, R.H.D.; Sharples, J.J.; Kablick, G.P., III. Pyrocumulonimbus pair in Wollemi and Blue Mountains National Parks, 22 November 2006. *Aust. Meteorol. Oceanogr. J.* **2012**, *62*, 117–126. [CrossRef]
30. Dowdy, A.J.; Fromm, M.D.; McCarthy, N. Pyrocumulonimbus lightning and fire ignition on Black Saturday in southeast Australia. *J. Geophys. Res. Atmos.* **2017**, *122*, 7342–7354. [CrossRef]
31. De Laat, A.T.J.; Stein Zweers, D.C.; Boers, R.; Tuinder, O.N. A solar escalator: Observational evidence of the self-lifting of smoke and aerosols by absorption of solar radiation in the February 2009 Australian Black Saturday plume. *J. Geophys. Res. Atmos.* **2012**, *117*. [CrossRef]
32. Pumphrey, H.C.; Santee, M.L.; Livesey, N.J.; Schwartz, M.J.; Read, W.G. Microwave Limb Sounder observations of biomass-burning products from the Australian bush fires of February 2009. *Atmos. Chem. Phys.* **2011**, *11*, 6285–6296. [CrossRef]
33. Siddaway, J.M.; Petelina, S.V. Transport and evolution of the 2009 Australian Black Saturday bushfire smoke in the lower stratosphere observed by OSIRIS on Odin. *J. Geophys. Res.* **2011**, *116*, D06203. [CrossRef]
34. Christian, K.; Yorks, J.; Das, S. Differences in the Evolution of Pyrocumulonimbus and Volcanic Stratospheric Plumes as Observed by CATS and CALIOP Space-Based Lidars. *Atmosphere* **2020**, *11*, 1035. [CrossRef]
35. Kablick, G.P., III; Allen, D.R.; Fromm, M.D.; Nedoluha, G.E. Australian pyroCb smoke generates synoptic-scale stratospheric anticyclones. *Geophys. Res. Lett.* **2020**, *47*, e2020GL088101. [CrossRef]

36. Khaykin, S.; Legras, B.; Bucci, S.; Sellitto, P.; Isaksen, L.; Tence, F.; Godin-Beekmann, S. The 2019/20 Australian wildfires generated a persistent smoke-charged vortex rising up to 35 km altitude. *Commun. Earth Environ.* **2020**, *1*, 1–12. [CrossRef]
37. Ohneiser, K.; Ansmann, A.; Baars, H.; Seifert, P.; Barja, B.; Jimenez, C.; Radenz, M.; Teisseire, A.; Floutsi, A.; Haarig, M.; et al. Smoke of extreme Australian bushfires observed in the stratosphere over Punta Arenas, Chile, in January 2020: Optical thickness, lidar ratios, and depolarization ratios at 355 and 532 nm. *Atmos. Chem. Phys.* **2020**, *20*, 8003–8015. [CrossRef]
38. Nolan, R.H.; Boer, M.; Collins, L.; Resco de Dios, V.; Clarke, H.; Jenkins, M.; Kenny, B.; Bradstock, R. Causes and consequences of eastern Australia's 2019–20 season of mega-fires. *Glob. Chang. Biol.* **2020**, *26*, 1039–1041. [CrossRef]
39. Boer, M.; Resco de Dios, V.; Bradstock, R.A. Unprecedented burn area of Australian mega forest fires. *Nat. Clim. Chang.* **2020**, *10*, 171–172. [CrossRef]
40. Kloss, C.; Sellitto, P.; Von Hobe, M.; Berthet, G.; Smale, D.; Krysztofiak, G.; Legras, B. Australian fires 2019–2020: Tropospheric and stratospheric pollution throughout the whole fire season. *Front. Environ. Sci.* **2021**, *9*, 220. [CrossRef]
41. Yu, P.; Davis, S.M.; Toon, O.B.; Portmann, R.W.; Bardeen, C.G.; Barnes, J.E.; Telg, H.; Maloney, C.; Rosenlof, K.H. Persistent Stratospheric Warming due to 2019–2020 Australian Wildfire Smoke. *Geophys. Res. Lett.* **2020**, *2020*, e2021GL092609.
42. Evans, L.F.; King, N.K.; MacArthur, D.A.; Packham, D.R.; Stephens, E.T. *Further Studies of the Nature of Bushfire Smoke*; Technical Paper; Division of Applied Organic Chemistry, Commonwealth Scientific and Industrial Research Organization: Canberra, ACT, Australia, 1976.
43. Harris, J.M.; Oltmans, S.J. Variations in tropospheric ozone related to transport at American Samoa. *J. Geophys. Res. Atmos.* **1997**, *102*, 8781–8791. [CrossRef]
44. Yamazaki, Y.; Matthias, V.; Miyoshi, Y.; Stolle, C.; Siddiqui, T.; Kervalishvili, G.; Laštovička, J.; Kozubek, M.; Ward, W.; Themens, D.R.; et al. September 2019 Antarctic sudden stratospheric warming: Quasi-6-day wave burst and ionospheric effects. *Geophys. Res. Lett.* **2020**, *47*, e2019GL086577. [CrossRef]
45. Clain, G.; Baray, J.L.; Delmas, R.; Diab, R.; de Bellevue, J.L.; Keckhut, P.; Posny, F.; Metzger, J.M.; Cammas, J.P. Tropospheric ozone climatology at two Southern Hemisphere tropical/subtropical sites, (Reunion Island and Irene, South Africa) from ozonesondes, LIDAR, and in situ aircraft measurements. *Atmos. Chem. Phys.* **2009**, *9*, 1723–1734. [CrossRef]
46. Randriambelo, T.; Baray, J.L.; Baldy, S.; Thompson, A.M.; Oltmans, S.; Keckhut, P. Lidar measurements of tropospheric ozone over Reunion Island: Influence of the synoptic situations. In Proceedings of the 2003 IEEE International Geoscience and Remote Sensing Symposium. Proceedings (IEEE Cat. No. 03CH37477), IEEE.IGARSS 2003, Toulouse, France, 21–25 July 2003; Volume 4, pp. 2311–2313.
47. Turquety, S.; Menut, L.; Siour, G.; Mailler, S.; Hadji-Lazaro, J.; George, M.; Clerbaux, C.; Hurtmans, D.; Coheur, P.-F. APIFLAME v2.0 biomass burning emissions model: Impact of refined input parameters on atmospheric concentration in Portugal in summer 2016. *Geosci. Model. Dev.* **2020**, *13*, 2981–3009. [CrossRef]
48. Bencherif, H.; Bègue, N.; Kirsch Pinheiro, D.; du Preez, D.J.; Cadet, J.M.; da Silva Lopes, F.J.; Clerbaux, C. Investigating the Long-Range Transport of Aerosol Plumes Following the Amazon Fires (August 2019): A Multi-Instrumental Approach from Ground-Based and Satellite Observations. *Remote Sens.* **2020**, *12*, 3846. [CrossRef]
49. Vigouroux, C.; Blumenstock, T.; Coffey, M.; Errera, Q.; García, O.; Jones, N.B.; De Mazière, M. Trends of ozone total columns and vertical distribution from FTIR observations at eight NDACC stations around the globe. *Atmos. Chem. Phys.* **2015**, *15*, 2915–2933. [CrossRef]
50. Zhou, M.; Langerock, B.; Vigouroux, C.; Sha, M.K.; Hermans, C.; Metzger, J.M.; Mazière, M.D. TCCON and NDACC CO measurements: Difference, discussion and application. *Atmos. Meas. Tech.* **2019**, *12*, 5979–5995. [CrossRef]
51. Mazière, M.D.; Thompson, A.M.; Kurylo, M.J.; Wild, J.D.; Bernhard, G.; Blumenstock, T.; Strahan, S.E. The Network for the Detection of Atmospheric Composition Change (NDACC): History, status and perspectives. *Atmos. Chem. Phys.* **2018**, *18*, 4935–4964. [CrossRef]
52. rPougatchev, N.S.; Connor, B.J.; Rinsland, C.P. Infrared measurements of the ozone vertical distribution above Kitt Peak. *J. Geophys. Res. Atmos.* **1995**, *100*, 16689–16697. [CrossRef]
53. Senten, C.; de Mazière, M.; Dils, B.; Hermans, C.; Kruglanski, M.; Neefs, E.; Scolas, F.; Vandaele, A.C.; Vanhaelewyn, G.; Vigouroux, C. Technical Note: New ground-based FTIR measure-ments at Ile de La Réunion: Observations, error analysis, and comparisons with independent data. *Atmos. Chem. Phys.* **2008**, *8*, 827–891. [CrossRef]
54. Rodgers, C.D. *Inverse Methods for Atmospheric Sounding: Theory and Practice, Series on Atmospheric, Oceanic and Planetary Physics—Vol. 2*; World Scientific Publishing Co.: Singapore, 2000.
55. Garcia, R.R.; Marsh, D.R.; Kinnison, D.E.; Boville, B.A.; Sassi, F. Simulation of secular trends in the middle atmosphere, 1950–2003. *J. Geophys. Res.* **2007**, *112*, D09301. [CrossRef]
56. Thompson, A.M.; Witte, J.C.; McPeters, R.D.; Oltmans, S.J.; Schmidlin, F.J.; Logan, J.A.; Fujiwara, M.; Kirchhoff, V.W.J.H.; Posny, F.; Coetzee, G.J.R.; et al. Southern Hemisphere Additional Ozonesondes (SHADOZ) 1998–2000 tropical ozone climatology: 1. Comparison with Total Ozone Mapping Spectrometer (TOMS) and ground-based measurements. *J. Geophys. Res.* **2003**, *108*, 8238. [CrossRef]
57. Komhyr, W.D.; Barnes, R.A.; Brothers, G.B.; Lathrop, J.A.; Opperman, D.P. Electrochemical concentration cell ozonesonde performance evaluation during STOIC 1989. *J. Geophys. Res. Atmos.* **1995**, *100*, 9231–9244. [CrossRef]

58. Thompson, A.; Witte, J.C.; Herman, G.J.; Oltmans, S.J.; Johnson, B.J.; Volker, W.J.; Kirchoff, V.W.J.H.; Schmidlin, F.J. Soutern Hemisphere Additionnal Ozonesonde (SHADOZ) 1998–2004 tropicale ozone climatology: 3. Instrumentation, station to station variability, and evaluation with simulated flight profiles. *J. Geophys. Res.* **2007**, *112*, D03304. [CrossRef]
59. Thompson, A.M.; Smit, H.G.; Witte, J.C.; Stauffer, R.M.; Johnson, B.J.; Morris, G.; Ogino, S.Y. Ozonesonde Quality Assurance: The JOSIE–SHADOZ (2017) Experience. *Bull. Am. Meteorol. Soc.* **2019**, *100*, 155–171. [CrossRef]
60. Boyd, I.S.; Bodeker, G.E.; Connor, B.J.; Swart, D.P.J.; Brinksma, E.J. An assessment of ECC ozonesondes operated using 1% and 0.5% KI cathode solutions at Lauder, New Zealand. *Geophys. Res. Lett.* **1998**, *25*, 2409–2412. [CrossRef]
61. Bodeker, G.E.; Boyd, I.S.; Matthews, W.A. Trends and variability in vertical ozone and temperature profiles measured by ozone sondes at Lauder, New Zealand: 1986–1996. *J. Geophys. Res.* **1998**, *103*, 28661–28681. [CrossRef]
62. Schoeberl, M.R.; Douglass, A.R.; Hilsenrath, E.; Bhartia, P.K.; Barnett, J.; Beer, R.; Waters, J.; Gunson, M.; Froidevaux, L.; Gille, J.; et al. Overview of the EOS Aura Mission, IEEE Trans. *Geosci. Remote Sens.* **2006**, *44*, 1066–1074. [CrossRef]
63. Livesey, N.J.; Read, W.G.; Wagner, P.A.; Froidevaux, L.; Lambert, A.; Manney, G.L.; Millán-Valle, L.F.; Pumphrey, H.C.; Santee, M.L.; Schwartz, M.J.; et al. *Version 4.2x Level 2 Data Quality and Description Document*; Version 4.2x-1.0; Tech. Rep. JPL D-33509; NASA Jet Propulsion Laboratory: La Cañada Flintridge, CA, USA, 2015.
64. Yan, X.; Wright, J.S.; Zheng, X.; Livesey, N.J.; Vömel, H.; Zhou, X. Validation of Aura MLS retrievals of temperature, water vapour and ozone in the upper troposphere and lower–middle stratosphere over the Tibetan Plateau during boreal summer. *Atmos. Meas. Tech.* **2016**, *9*, 3547–3566. [CrossRef]
65. Clarisse, L.; R'Honi, Y.; Coheur, P.-F.; Hurtmans, D.; Clerbaux, C. Thermal infrared nadir observations of 24 atmospheric gases. *Geophys. Res. Lett.* **2011**, *38*, L10802. [CrossRef]
66. Clerbaux, C.; Boynard, A.; Clarisse, L.; George, M.; Hadji-Lazaro, J.; Herbin, H.; Hurtmans, D.; Pommier, M.; Razavi, A.; Turquety, S. Monitoring of atmospheric composition using the thermal infrared IASI/MetOp sounder. *Atmos. Chem. Phys.* **2009**, *9*, 6041–6054. [CrossRef]
67. Coheur, P.-F.; Clarisse, L.; Turquety, S.; Hurtmans, D.; Clerbaux, C. IASI measurements of reactive trace species in biomass burning plumes. *Atmos. Chem. Phys.* **2009**, *9*, 5655–5667. [CrossRef]
68. Hurtmans, D.; Coheur, P.F.; Wespes, C.; Clarisse, L.; Scharf, O.; Clerbaux, C.; Hadji-Lazaro, J.; George, M.; Turquety, S. FORLI radiative transfer and retrieval code for IASI. *J. Quant. Spectrosc. Radiat. Transf.* **2012**, *113*, 1391–1408. [CrossRef]
69. Boynard, A.; Hurtmans, D.; Garane, K.; Goutail, F.; Hadji-Lazaro, J.; Koukouli, M.E.; Wespes, C.; Vigouroux, C.; Keppens, A.; Pommereau, J.-P. Validation of the IASI FORLI/EUMETSAT ozone products using satellite (GOME-2), ground-based (Brewer–Dobson, SAOZ, FTIR) and ozonesonde measurements. *Atmos. Meas. Tech.* **2018**, *11*, 5125–5152. [CrossRef]
70. Safieddine, S.; Boynard, A.; Coheur, P.F.; Hurtmans, D.; Pfister, G.; Quennehen, B.; Clerbaux, C. Summertime tropospheric ozone assessment over the Mediterranean region using the thermal infrared IASI/MetOp sounder and the WRF-Chem model. *Atmos. Chem. Phys.* **2014**, *14*, 10119–10131. [CrossRef]
71. Safieddine, S.; Boynard, A.; Hao, N.; Huang, F.; Wang, L.; Ji, D.; Clerbaux, C. Tropospheric ozone variability during the East Asian summer monsoon as observed by satellite (IASI), aircraft (MOZAIC) and ground stations. *Atmos. Chem. Phys.* **2016**, *16*, 10489–10500. [CrossRef]
72. Yang, X.; Zhao, C.; Yang, Y. Long-term multi-source data analysis about characteristics of aerosol optical properties and types over Australia. *Atmos. Chem. Phys. Discuss.* **2020**. [CrossRef]
73. Holben, B.N.; Eck, T.F.; Slutsker, I.; Tanré, D.; Buis, J.P.; Setzer, A.; Vermote, E.; Reagan, J.A.; Kaufman, Y.J.; Nakajima, T.; et al. AERONET—A federated instrument network and data archive for aerosol characterization. *Remote Sens. Environ.* **1998**, *66*, 11. [CrossRef]
74. Dubovik, O.; King, M.D. A flexible inversion algorithm for retrieval of aerosol optical properties from Sun and sky radiance measurements. *J. Geophys. Res.* **2000**, *105*, 20673–20696. [CrossRef]
75. Dubovik, O.; Sinyuk, A.; Lapyonok, T.; Holben, B.N.; Mishchenko, M.; Yang, P.; Eck, T.F.; Volten, H.; Muñoz, O.; Veihelman Van der Zande, W.J.; et al. Application of spheroid models to account for aerosol particle non sphericity in remote sensing of desert dust. *J. Geophys. Res.* **2006**, *111*, D11208. [CrossRef]
76. Giles, D.M.; Sinyuk, A.; Sorokin, M.G.; Schafer, J.S.; Smirnov, A.; Slutsker, I.; Welton, E.J. Advancements in the Aerosol Robotic Network (AERONET) Version 3 database—Automated near-real-time quality control algorithm with improved cloud screening for Sunphotometer aerosol optical depth (AOD) measurements. *Atmos. Meas. Tech.* **2019**, *12*, 169–209. [CrossRef]
77. Logothetis, S.A.; Salamalikis, V.; Kazantzidis, A. Aerosol classification in Europe, Middle East, North Africa and arabian Peninsula based on AERONET version 3. *Atmos. Res.* **2020**, *239*, 104893. [CrossRef]
78. Wolters, E.; Toté, C.; Sterckx, S.; Adriaensen, S.; Henocq, C.; Bruniquel, J.; Dransfeld, S. iCOR Atmospheric Correction on Sentinel-3/OLCI Over Land: Intercomparison with AERONET, RadCalNet, and SYN Level-2. *Remote Sens.* **2021**, *13*, 654. [CrossRef]
79. Winker, D.M.; Tackett, J.L.; Getzewich, B.J.; Liu, Z.; Vaughan, M.A.; Rogers, R.R. The global 3-D distribution of tropospheric aerosols as characterized by CALIOP. *Atmos. Chem. Phys.* **2013**, *13*, 3345–3361. [CrossRef]
80. Young, S.A.; Vaughan, M.A.; Garnier, A.; Tackett, J.L.; Lambeth, J.D.; Powell, K.A. Extinction and optical depth retrievals for CALIPSO's Version 4 data release. *Atmos. Meas. Tech.* **2018**, *11*, 5701–5727. [CrossRef]
81. Kim, M.H.; Omar, A.H.; Tackett, J.L.; Vaughan, M.A.; Winker, D.M.; Trepte, C.R.; Magill, B.E. The CALIPSO version 4 automated aerosol classification and lidar ratio selection algorithm. *Atmos. Meas. Tech.* **2018**, *11*, 6107–6135. [CrossRef]

82. Mehta, M.; Khushboo, R.; Raj, R.; Singh, N. Spaceborne observations of aerosol vertical distribution over Indian mainland (2009–2018). *Atmos. Environ.* **2021**, *244*, 117902. [CrossRef]
83. Yu, H.; Tan, Q.; Chin, M.; Remer, L.A.; Kahn, R.A.; Bian, H.; Kim, D.; Zhang, Z.; Yuan, T.; Omar, A.H.; et al. Estimates of African dust depositionalong the trans-Atlantic transit usingt he decadelong record of aerosolmeasurements from CALIOP, MODIS, MISR, and IASI. *J. Geophys. Res. Atmos.* **2019**, *124*, 7975–7996. [CrossRef] [PubMed]
84. Zabukoveck, A.; Ancellet, G.; Penner, I.E.; Arshinov, M.; Kozlov, V.; Pelon, J.; Paris, J.-D.; Kokhanenko, G.; Balin, Y.S.; Chernov, D.; et al. Characterization of Aerosol Sources and Optical Properties in Siberia Using Airborne and Spaceborne Observations. *Atmosphere* **2021**, *12*, 244. [CrossRef]
85. Hassinen, S.; Balis, D.; Bauer, H.; Begoin, M.; Delcloo, A.; Eleftheratos, K.; Zyrichidou, I. Overview of the O3M SAF GOME-2 operational atmospheric composition and UV radiation data products and data availability. *Atmos. Meas. Tech.* **2016**, *9*, 383–407. [CrossRef]
86. Giglio, L.; Schroeder, W.; Justice, C.O. The collection 6 MODIS active fire detection algorithm and fire products. *Remote Sens. Environ.* **2016**, *178*, 31–41. [CrossRef] [PubMed]
87. Kaufman, Y.J.; Justice, C.O.; Flynn, L.P.; Jendall, J.D.; Prins, E.M.; Giglio, L.; Ward, D.E.; Menzel, W.P.; Setzer, A.W. Monitoring global fire monitoring from EOS-MODIS. *J. Geophys. Res.* **1998**, *103*, 32315–32338.
88. Australian Government, B.o.M: Special Climate Statement 72—Dangerous bushfire weather in spring 2019. Available online: https://www.bom.gov.au/climate/current/statements/scs67.pdf (accessed on 18 December 2019).
89. Lawson, S.J.; Keywood, M.D.; Galbally, I.E.; Gras, J.L.; Cainey, J.M.; Cope, M.E.; Krummel, P.B.; Fraser, P.J.; Steele, L.P.; Bentley, S.T.; et al. Biomass burning emissions of trace gases and particles in marine air at Cape Grim, Tasmania. *Atmos. Chem. Phys. Discuss.* **2015**, *15*, 13393–13411. [CrossRef]
90. Mitchell, R.M.; Forgan, B.W.; Campbell, S.K. The Climatology of Australian Aerosol. Atmospheric Chem. *Phys. Discuss.* **2017**, *17*, 5131–5154. [CrossRef]
91. Qin, Y.; Mitchell, R.M. Characterisation of episodic aerosol types over the Australian continent. *Atmos. Chem. Phys.* **2009**, *9*, 1943–1956. [CrossRef]
92. Mukkavilli, S.; Prasad, A.; Taylor, R.; Huang, J.; Mitchell, R.; Troccoli, A.; Kay, M. Assessment of atmospheric aerosols from two reanalysis products over Australia. *Atmos. Res.* **2019**, *215*, 149–164. [CrossRef]
93. Yang, X.; Zhao, C.; Yang, Y.; Yan, X.; Fan, H. Statistical aerosol properties associated with fire events from 2002 to 2019 along with a case analysis in 2019 over Australia. *Atmos. Chem. Phys. Discuss.* **2021**, *21*, 3833–3853. [CrossRef]
94. Torres, O.; Jethva, H.; Ahn, C.; Jaross, G.; Loyola, D.G. TROPOMI aerosol products: Evaluation and observations of synoptic-scale carbonaceous aerosol plumes during 2018–2020. *Atmos. Meas. Tech.* **2020**, *13*, 6789–6806. [CrossRef]
95. World Meteorological Organization. *International Meteorological Vocabulary*, 2nd ed.; World Meteorological Organization: Geneva, Switzerland, 1992; Available online: https://www.wmo.int/e-catalog/detail_en.php?PUB_ID=402 (accessed on 10 January 2021).
96. Griffith, D.W.T.; Jones, N.B.; Matthews, W.A. Interhemispheric ratio and annual cycle of carbonyl sulfide (OCS) total column from ground-based solar FTIR spectra. *J. Geophys. Res. Space Phys.* **1998**, *103*, 8447–8454. [CrossRef]
97. Sakai, T.; Uchino, O.; Nagai, T.; Liley, B.; Morino, I.; Fujimoto, T. Long-term variation of stratospheric aerosols observed with lidars over Tsukuba, Japan, from 1982 and Lauder, New Zealand, from 1992 to 2015. *J. Geophys. Res. Atmos.* **2016**, *121*, 10283–10293. [CrossRef]
98. McKeen, S.A.; Wotawa, G.; Parrish, D.D.; Holloway, J.S.; Buhr, M.P.; Hübler, G.; Fehsenfeld, F.C.; Meagher, J.F. Ozone production from Canadian wildfires during June and July of 1995. *J. Geophys. Res. Atmos.* **2002**, *107*, ACH 7-1–ACH 7-25. [CrossRef]
99. Stevenson, D.S.; Dentener, F.J.; Schultz, M.G.; Ellingsen, K.; Van Noije, T.P.C.; Wild, O.; Zeng, G.; Amann, M.; Atherton, C.S.; Bergmann, D.J.; et al. Multimodel ensemble simulations of present-day and near-future tropospheric ozone. *J. Geophys. Res. Atmos.* **2006**, *111*. [CrossRef]
100. Baylon, P.; Jaffe, D.A.; Wigder, N.L.; Gao, H.; Hee, J. Ozone enhancement in western US wildfire plumes at the Mt. Bachelor Observatory: The role of Nox. *Atmos. Environ.* **2015**, *109*, 297–304. [CrossRef]
101. Wigder, N.L.; Jaffe, D.A.; Saketa, F.A. Ozone and particulate matter enhancements from regional wildfires observed at Mount Bachelor during 2004–2011. *Atmos. Environ.* **2013**, *75*, 24–31. [CrossRef]
102. Arnold, S.R.; Emmons, L.K.; Monks, S.A.; Law, K.S.; Ridley, D.A.; Turquety, S.; Long, Y. Biomass burning influence on high-latitude tropospheric ozone and reactive nitrogen in summer 2008: A multi-model analysis based on POLMIP simula-tions. *Atmos. Chem. Phys.* **2015**, *15*, 6047–6068. [CrossRef]
103. Jaffe, D.A.; Wigder, N.L. Ozone production from wildfires: A critical review. *Atmos. Environ.* **2012**, *51*, 1–10. [CrossRef]
104. Parrington, M.; Palmer, P.I.; Lewis, A.; Lee, J.D.; Rickard, A.R.; Di Carlo, P.; Taylor, J.W.; Hopkins, J.R.; Punjabi, S.; Oram, D.E.; et al. Ozone photochemistry in boreal biomass burning plumes. *Atmos. Chem. Phys. Discuss.* **2013**, *13*, 7321–7341. [CrossRef]
105. Mauzerall, D.L.; Logan, J.A.; Jacob, D.J.; Anderson, B.E.; Blake, D.R.; Bradshaw, J.D.; Heikes, B.; Sachse, G.W.; Singh, H.; Talbot, B. Photochemistry in biomass burning plumes and implications for tropospheric ozone over the tropical South At-lantic. *J. Geophys. Res. Atmos.* **1998**, *103*, 8401–8423. [CrossRef]
106. Jonquieres, I.; Marenco, A.; Maalej, A.; Rohrer, F. Study of ozone formation and transatlantic transport from biomass burning emissions over West Africa during the airborne tropospheric ozone campaigns TROPOZ I and TROPOZ II. *J. Geophys. Res.-Atmos.* **1998**, *103*, 19059–19073. [CrossRef]

107. Sanhueza, E.; Crutzen, P.J.; Fernandez, E. Production of boundary layer ozone from tropical American savannah biomass burning emissions. *Atmos. Environ.* **1999**, *33*, 4969–4975. [CrossRef]
108. Baray, J.L.; Duflot, V.; Posny, F.; Cammas, J.P.; Thompson, A.M.; Gabarrot, F.; Zeng, G. One year ozonesonde meas-urements at Kerguelen Island (49.2° S, 70.1° E): Influence of stratosphere-to-troposphere exchange and long-range transport of biomass burning plumes. *J. Geophys. Res. Atmos.* **2012**, *117*. [CrossRef]
109. Engel, C.B.; Lane, T.P.; Reeder, M.J.; Rezny, M. The meteorology of Black Saturday. *Q. J. R. Meteorol. Soc.* **2012**, *139*, 585–599. [CrossRef]